Nanoscale

ROYAL SOCIETY OF CHEMISTRY

REVIEW

View Article Online
View Journal | View Issue

Check for updates

Cite this: *Nanoscale*, 2022, **14**, 2885

# Two-dimensional copper based colloidal nanocrystals: synthesis and applications

Nilotpal Kapuria, Niraj Nitish Patil, Kevin M. Ryan and Shalini Singh *

Two-dimensional (2D) semiconductor nanocrystals display unconventional physical and opto-electronic properties due to their ultrathin and unique electronic structures. Since the success of Cd-based photoemissive nanocrystals, the development of sustainable and low-cost nanocrystals with enhanced electronic and physical properties has become a central research theme. In this context, copper-based semiconductor 2D nanocrystals, the cost-effective and eco-friendly alternative, exhibit unique plasmonic resonance, transport properties, and high ionic conductivity beneficial for sensing, energy storage, conversion, and catalytic applications. This review summarizes recent progress in the colloidal synthesis, growth mechanisms, properties, and applications of 2D copper-based nanostructures with tunable compositions, dimensions, and crystal phases. We highlight the growth mechanisms concerning their shape evolution in two dimensions. We analyse the effectiveness of cation exchange as a tool to synthesize multinary nanocrystals. Based on the preparation of Cu-based chalcogenide and non-chalcogenide compositions, we discuss synthesis control achieved *via* colloidal approaches to allow dimension tunability, phase engineering, and plasmonic and thermoelectric property optimization. Furthermore, their potential in various applications of catalysis, energy storage, and sensing is reviewed. Finally, we address the current challenges associated with 2D Cu-based nanocrystal development and provide an outlook pertaining to unexplored research areas.

Received 21st October 2021,
Accepted 22nd January 2022

DOI: 10.1039/d1nr06990j

rsc.li/nanoscale

Open Access Article. Published on 27 January 2022. Downloaded on 11/30/2025 6:59:56 AM.
This article is licensed under a Creative Commons Attribution 3.0 Unported Licence.

*Department of Chemical Sciences and Bernal Institute, University of Limerick, Limerick, Ireland. E-mail: Shalini.Singh@ul.ie*

**Shalini Singh**

*Dr Shalini Singh is a Lecturer at the Department of Chemical Sciences and the Bernal Institute at the University of Limerick, Ireland. She received her PhD in chemistry from the University of Limerick in 2016 and was an FWO (Research Foundation, Flanders, Belgium) Postdoctoral Fellow at Ghent University, Belgium until 2019. Since 2020, she has been leading the Functional Nanomaterial Research Group at the University of Limerick. Her research interest is focused on the development of novel colloidal semiconductor and metallic nanocrystals for energy conversion and storage applications.*

## 1. Introduction

The advances in colloidal synthesis approaches over the past decade have resulted in unprecedented synthesis control over several solution-processed two-dimensional (2D) nanocrystals (NCs), with layered and non-layered structures, that display extraordinary physical and optoelectronic properties.[1–8] In the layered structures, each monolayer with a covalently bonded atomic arrangement is vertically stacked together *via* the weak van der Waals (vdW) force. Using colloidal approaches, a range of layered transition metal chalcogenides of $ME_2$ (M = Mo, W, Zr, Hf), SnS, GeS, InS, and GaS have been successfully synthesised.[1,3,9–12] Controlling the 2D thickness of these nanostructures resulted in high mechanical stability, optical transparency, the transition of indirect to direct bandgap, and stabilisation of metastable phases. The non-layered structures possess covalent bonds in three dimensions. For non-layered NCs, the 2D nature is defined by strong electron–hole confinement in one dimension or by growth limitation in one of the directions. Quantum confinement resulting from controlling the thickness below the Bohr radius leads to several exciting optoelectronic properties such as sharp emissions, large laser threshold, enhanced oscillator strength, fast exciton dynamics, *etc*. Colloidal nanosheets, nanobelts, or rectangular nanoplate-

Open Access Article. Published on 27 January 2022. Downloaded on 11/30/2025 6:59:56 AM.
This article is licensed under a Creative Commons Attribution 3.0 Unported Licence.

lets of CdE, ZnE, PbS, PbSe, HgSe, and HgTe are among the most explored systems in this category.[6,13–20]

The sustainability and toxicity issues associated with heavy elements constituting a significant portion of nanomaterials (*e.g.* Cd and Pb) have shifted the current research focus towards cost-effective and eco-friendly NCs with a 2D morphology such as copper chalcogenides, copper phosphide ($Cu_{3-x}P$), and metallic alloys.[21–26] Owing to their high electron conductivity and thickness controlled optoelectronic properties, they have found applications in thermoelectrics, alkali-ion battery, sensing, *etc.*[27–31] These NCs with a 2D morphology also exhibit a high surface area for efficient catalysis and further allow the manipulation of plasmonic properties by doping, defect engineering, or heterostructure formation.[32] For the semiconductor and metallic NCs that do not display quantum confinement, the 2D shape is largely defined by the morphological appearance in the form of discs, plates, or sheets (Scheme 1a). The nanocrystals with high symmetry, such as hexagonal, are more inclined to form hexagonal and triangular plates, or discs, and NCs with cubic or orthorhombic crystal structures tend to form platelets. In terms of quantum confinement, nanosheets display strong out of plane confinement and zero in-plane confinement as the length and width of nanosheets are at least 20 times larger than the thickness,[6,21] whereas nanoplatelets display weak electron confinement along the width and length.[7] Likewise, nanodiscs and nanoplates exhibit weak in-plane electron confinement. For nanoplates and nanodiscs confinement along the vertical direction can range from weak to strong depending on the thickness. The least passivated narrow edges of these 2D NCs are often critical for active species binding during electrochemical reactions.

The emerging ternary alkali metal (Cs, Rb) copper halides that display strong electron–phonon coupling and structural distortion upon photoexcitation result in deeply self-trapped emission.[33,34] Given their photoluminescence properties, they are applied in blue LED fabrication. Moreover, they are also predicted as phonon glass electron crystals with a thermoelectric figure of merit ~ 2.6.[35] In addition, the high ionic mobility of $Cu^+$ in a Cu-based NC lattice benefits foreign cation substitution forming multinary NCs, which is not feasible for most other 2D NCs.[36,37] These Cu-based NCs can possess both layered and non-layered structures. For example, in orthorhombic $CuSbS_2$ each layer of interconnected $CuS_3$ and $SbS_2$ chains weakly interacts *via* the vdW force.[27] Interestingly, a layered copper sulphide that exhibits temperature-dependent

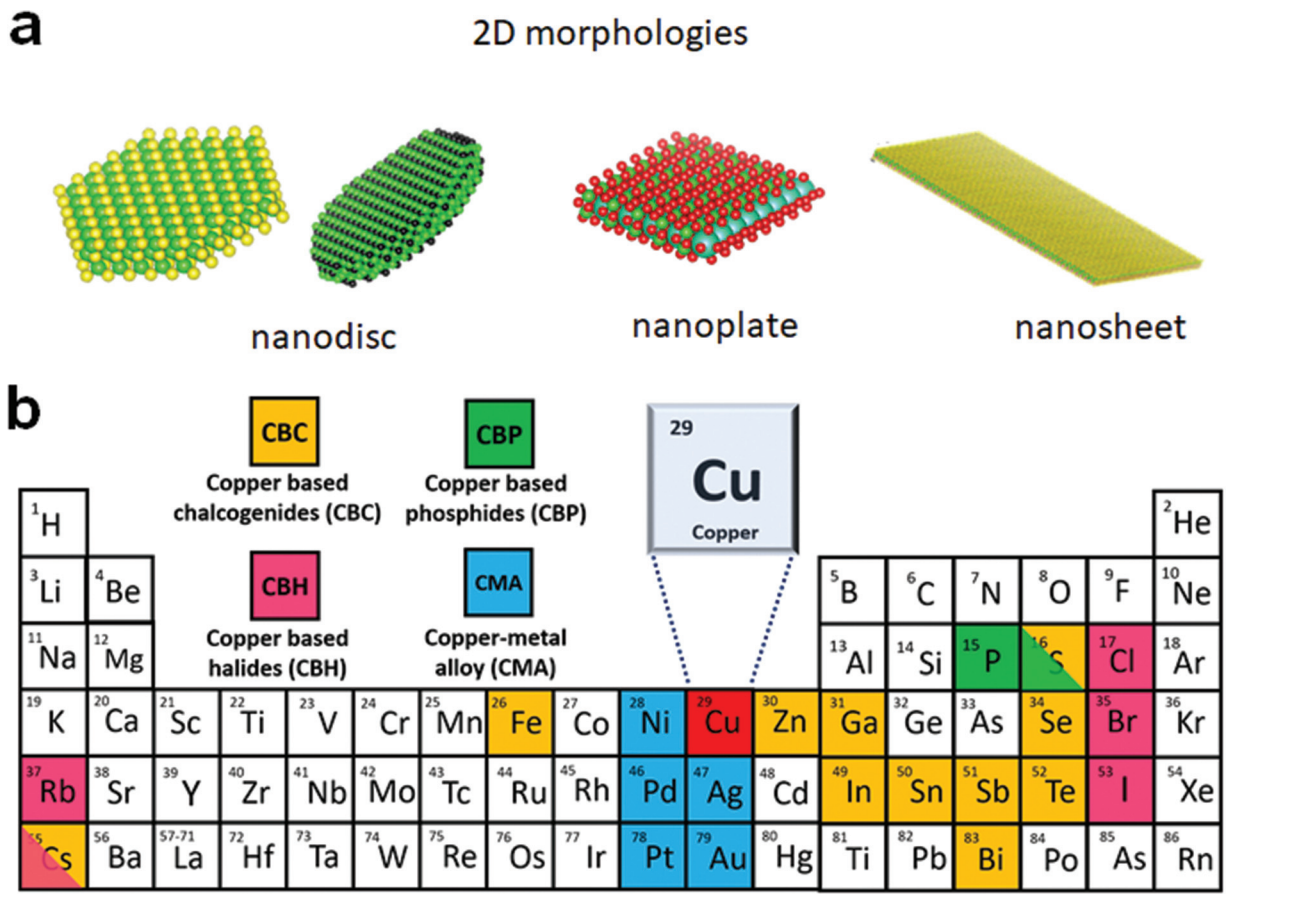


Scheme 1 (a) Possible morphologies of colloidal 2D NCs where charge carriers are confined within a plane but can move along the plane; (b) composition of Cu-based 2D NCs.

 This journal is © The Royal Society of Chemistry 2022

Open Access Article. Published on 27 January 2022. Downloaded on 11/30/2025 6:59:56 AM.
This article is licensed under a Creative Commons Attribution 3.0 Unported Licence.

photoluminescence exists constituting monolayers of two $(Cu–S)_n$ chains interconnected by Cu–Cu bonds, and where each layer is interconnected by alkanethiol.[38] Given the significant advancement of synthesis control and applicability of the colloidal Cu-based 2D NCs that have been achieved to date, it is timely to review the progress made, challenges remaining, and future outlook.

The present review aims at providing an overview of the multifaceted advancements that have emerged in the growth mechanism, synthesis, properties, and application of colloidal 2D Cu based NCs. First, we briefly discuss the various compositions of 2D Cu based NCs achieved using colloidal approaches. We discuss the growth mechanism of these NCs, highlighting the effect of ligand passivation, the effect of alkanethiol and halide anions in copper chalcogenide formation and cation exchange for multi-elemental NC formation. This is followed by the discussion on synthesis and growth parameters, with a specific focus on copper-based chalcogenides, copper phosphides, copper-based halide NCs, and metal NCs. We describe their plasmonic and thermoelectric properties and applications in photocatalysis, electrocatalysis, energy storage, and sensors. We conclude the review with an outlook of the different synthetic approaches and compositions for 2D copper based NCs in view of their applications.

## 2. Colloidal 2D copper based NCs

In recent years, bottom-up approaches have gained prominence in synthetic chemistry, particularly with the advancement of synthetic techniques for producing nanomaterials with well-defined size, morphology, phase, and characteristics.[39,40] So far, bottom-up methods, such as the physical deposition method and wet chemical synthesis, have been comprehensively investigated to develop 2D nanostructures.[8,41] In particular, colloidal synthesis approaches have shown significant utility in synthesising solution processable 2D NCs with the morphology ranging from nanosheets, nanodiscs to nanoplates.[40,42,43] In a typical colloidal synthesis, the organic anions and metal salts or organometallic precursors as metal sources are combined with the organic solvent with boiling point up to 360 °C under inert conditions. The heat-up technique and the hot injection approach are the two ways often used in colloidal systems. The heat-up technique includes gradually heating the precursors in the presence of ligands and organic solvents.[44] In contrast, the hot injection method induces supersaturation by creating a temperature gradient between anionic and metal precursors. The rapid injection of an anionic source into a hot metal precursor solution in the presence of ligands and organic solvents, or *vice versa*, starts the nucleation.[45,46] Heat-up synthesis is beneficial for the gram-scale synthesis of NCs due to its simplicity. However, in the heat-up process, the nucleation and growth step are not separated well due to the continuous supply of the monomer with an increment of thermal energy. The extended monomer saturation stage induces broad size distribution, especially for multinary systems. In contrast, hot-injection induces a supersaturation that accounts for single burst nucleation providing more control over the shape, size, and composition.

To date, using colloidal approaches, a number of 2D NCs of binary and multinary Cu chalcogenides ($Cu_{2-x}E$, E = S, Se, Te), binary Cu phosphides ($Cu_{3-x}P$) and Cu–metal alloys (Scheme 1b) have been synthesised. The binary $Cu_{2-x}S$, $Cu_{2-x}Se$, $Cu_{2-x}Te$, and $Cu_{3-x}P$ are the most explored compositions for 2D morphologies.[47–50] The introduction of group III metals such as In and Ga in the binary Cu chalcogenides resulted in the second most explored compositions of ternary $CuInS_2$ and $CuGaS_2$ and their selenide alternatives in 2D mrophology.[51–53] Here the partial replacement of In for Ga and S for Se has resulted in quaternary compositions of $CuIn_{1-x}Ga_xS_2$, $CuInS_{2x}Se_{2-2x}$ and a more complex composition of $CuIn_{1-x}Ga_xS_{2x}Se_{2-2x}$.[54] Introduction of transition metals, group IV and group V elements into Cu-chalcogenide 2D NCs resulted in the following compositions of $CuSbS_2$, $Cu_3SbS_3$, $Cu_3BiS_3$, $Cu_2SnS_3$, $Cu_2SnSe_3$, $Cu_2GeS_3$, $CuFeS_2$, $Cu_2SnZnSe_4$, $Cu_2GeZnSe_4$, *etc.*[22,37,55–61] More recently, metal halides of Cu with compositions of $Cs_3Cu_2I_5$, $Cs_3Cu_2Br_5$ and $Rb_2CuX_3$ (X = Cl, Br) have also been synthesised.[35,62] Among the metallic Cu 2D NCs seeded growth materialised NCs with PdCu and PdPtCu compositions.[63] Apart from these, many other unconventional compositions such as $Cu_3P_{1-x}S_x$ and $CsCu_5S_3$ have also been achieved using colloidal methods.[64,65] All the compositional outcomes that are achieved using the colloidal approach are highlighted in Scheme 1b.

2D NCs of $Cu_{2-x}S$, $Cu_{2-x}Se$, $Cu_{3-x}P$, and $Cu_{2-x}Te$ have been synthesised using heat-up and hot-injection approaches in different phases.[23,47,48,66–69] They are mainly investigated for their plasmonic and electronic properties. Though initial approaches for synthesising binary $Cu_{2-x}S$ were solely based on traditional hot-injection and heat-up techniques, later soft templates of Cu-thiolates and other amphiphilic ligands were improvised to achieve NCs with ultrathin thickness. For binary $Cu_{3-x}P$, heat up techniques are devised based on the decomposition of organophosphorous compounds such as trioctylphosphine, tris(diethylamino)phosphine and triphenyl phosphite. High temperatures above 300 °C are used for trioctylphosphine but other precursors could be decomposed below 300 °C. While the hot-injection synthesis of $Cu_{3-x}P$ requires the injection of highly reactive precursors such as tris(trimethylsilyl) phosphine. Among the other semiconductor NCs are multinary $CuInS_2$ nanodiscs, nanosheets, $CuSbS_2$ nanosheets, and $Cu_3BiS_3$ nanoplatelets using heat-up and hot-injection approaches.[21,52,55,56,70] Initial approaches for synthesising $CuInS_2$ were based on the heat-up of the metal precursor and S source. But extension of the elemental composition to quaternary by the introduction of Ga and Se required a more controlled hot-injection approach where cation and anion introduction windows can be separated based on the injection temperature. For group V based NCs, heat up techniques are based on the decomposition of diethyldithiocarbamate precursors of metals.[55,56] Using the cation exchange of $Cu_{2-x}S$ and

Open Access Article. Published on 27 January 2022. Downloaded on 11/30/2025 6:59:56 AM.
This article is licensed under a Creative Commons Attribution 3.0 Unported Licence.

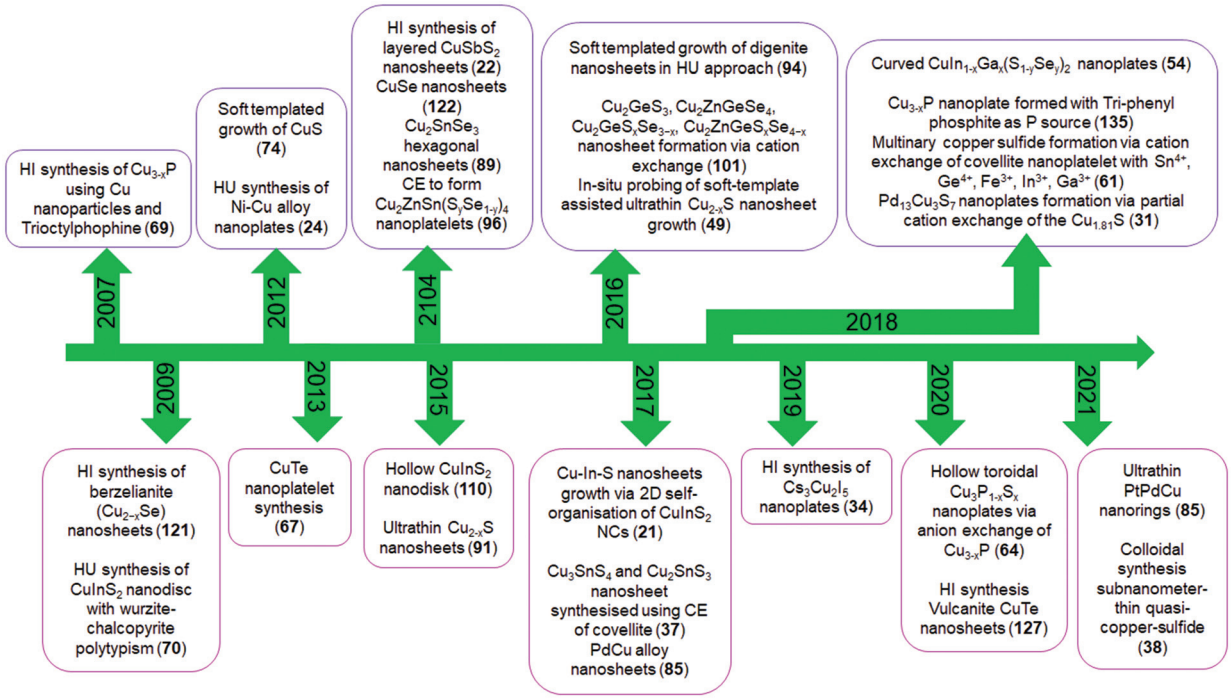


**Scheme 2** Literature reports on colloidal 2D Cu-based nanocrystals. Here HI, HU and CE denote hot-injection, heat-up and cation exchange, respectively.

$Cu_{2-x}Se$ 2D templates several heterostructures and multinary nanoplates with more complex compositions involving Au, Ag, Cd, Zn, Hg, Pb, Pd, In, Ga, Fe, Sn, and Ge have also been achieved in recent times.[61] The recent addition to the ion exchange series is the anion exchange of the $Cu_{3-x}P$ template for the materialisation of $Cu_3P_{1-x}S_x$ nanorings.[64] Alloyed Cu-based multimetallic NCs such as PtPdCu nanorings have also been synthesised *via* $Cu^{2+}$ introduction of the PtPd template.[63] The milestones achieved in terms of synthesis in this field are highlighted in Scheme 2.

## 3. Growth mechanism

Controlling the morphology in two dimensions in the form of colloidal nanoplates, nanodiscs, or nanosheets is generally achieved through oriented attachments, soft template-assisted growth, cation exchange (CE) of 2D templates or due to the ligand passivation of certain facets and restriction from crystal symmetry.[6,21] In oriented attachment/self-organisation, the energetically under-passivated crystal facets of NCs attach to form a superstructure assembly which further goes through recrystallisation to form larger nanocrystals.[71–73] However, the 2D morphology will form when the preferential binding of ligands to the facet perpendicular to the growth facet constricts the assembly in a two-dimensional template. In the oriented attachment driven growth of 2D nanocrystals, Schliehe *et al.* describe an egg tray-like assembly of PbS quantum dots *via* attachment of (110) facets where the oleic acid bound to the (100) facets formed a bilayer stacking resulting in PbS nanosheets.[73] The surface energy is a controlling parameter to decide the shape of NCs in solution. The Gibbs free energy for an individual NC formation is described as $\Delta G = \Delta G_{bulk} + \gamma\delta A$, where $\Delta G_{bulk} = \Delta H_{bulk} - T\Delta S_{bulk}$, $\gamma$ is the surface energy per unit area of NCs and $A$ is the total area of NC. The surface energy ($\gamma$) contributes significantly to the total Gibbs free energy for NC formation. The surface energy of individual NCs depends on the passivation of certain facets, and the ligands play a critical role in determining which facets will grow. Therefore, ligand passivation is regarded as a significant driving factor for forming anisotropic NCs.[7] In the case of soft templated growth, ligands such as OLA and 1-DDT, or an amphiphilic surfactant such as cetrimonium bromide that dissolve the cationic precursors can form lamellar templates sandwiching the metal cations between the top and bottom layer alkyl chain coordinated *via* their functional groups.[74] The stability of such a lamellar structure facilitates metal chalcogenide formation in the 2D confined framework upon the introduction of anionic precursors.[74–76] Another method, the cation exchange, which requires topotactic cationic replacement of 2D template NCs to form a new composition, has also been used to synthesize several multinary 2D NCs from 2D binary metal chalcogenide templates.[77] The formation of anisotropic metal nanocrystals proceeds *via* a slow reduction process, providing a better chance of overcoming the more thermodynamically favored reactions toward forming truncated nanocubes due to their intrinsically higher energy compared to other isotropic shapes.[78,79] Additionally, the aniso-

 This journal is © The Royal Society of Chemistry 2022

Open Access Article. Published on 27 January 2022. Downloaded on 11/30/2025 6:59:56 AM. This article is licensed under a Creative Commons Attribution 3.0 Unported Licence.

tropic growth of multimetallic metal NCs is vastly influenced by the nature and shape of the initial seeds.[80,81] In contrast to semiconductors, the seeded growth of multi-metallic NCs initiates *via* the deposition of foreign cations on the seed and their subsequent interatomic diffusion forms the alloy. The following sub-sections will discuss the crucial mechanisms that drive the growth and 2D morphology evolution in the colloidal synthesis of Cu based NCs.

### 3.1. Effect of ligand passivation

In colloidal synthesis the choice of the ligand is a crucial factor in directing the shape of NCs during growth. Depending on the metal–anion framework of the terminating facets, the polarity of each facet varies; thus, the surface energy is also different for each facet.[82,83] The strong binding of the ligand to certain facets inhibits monomer deposition on those facets compared to other facets and influences anisotropic growth. The ligands can be small molecules generated upon precursor decomposition such as halides, carbonyls, solvents such as oleylamine (OLA), trioctylphosphine oxide (TOPO), or metal–ligand complexes.[51,84] During the growth of metal NCs with the cubic crystal phase, CO generated upon metal carbonyl precursor decomposition binds explicitly with the (111) facet to inhibit further monomer deposition from forming 2D NCs enclosed with {111} planes. For example, Yang *et al.* used $Mo(CO)_6$ for generating CO *in situ*, which influenced the nanosheet morphology during CuPd NC growth.[85] As another class of small molecules, halide ions act as surface-active species that govern the shape of NCs. The halide ions can influence the anisotropic development of metal nanocrystals in numerous ways, including modification of the redox potentials of the metal ions, serving as face-specific capping agents, and/or influencing the degree of metal underpotential deposition at the nanocrystal surface. For example, the presence of halide ions was shown to control the 2D morphology in hexagonal $CuInS_2$ and $CuGaS_2$ NCs.[52,86,87] Liu *et al.* showed the formation of 2D $CuGaS_2$ NCs by using $GaCl_3$ as the $Ga^{3+}$ source whereas an identical synthesis involving Ga(acetylacetonate) [$Ga(acac)_3$] formed nanorods.[52] The favourable adsorption of $Cl^-$ on basal {001} facets of wurtzite $CuGaS_2$ influenced the 2D growth (Fig. 5e and f). Tang *et al.* demonstrated the influence of halide ions on the morphology-controlled synthesis of Cu nanocrystals in the aqueous phase.[88] The type of halide ion ($Cl^-$, $Br^-$, $I^-$) solely controlled the morphology of nanocrystals (2D plates, 1D wires, and 3D polyhedral particle). DFT study showed that the co-adsorption strength of ammonium and halide ions on Cu(100) compared to Cu(111) was a critical factor in regulating the shape of the Cu NCs. As a result, the selective adsorption of halide ions on certain facets of Cu NCs would contribute to morphological differences.

Coordinating ligands can affect the NC morphology immensely by adsorbing onto partially charged facets. OLA was shown to passivate the polar (001) facet of wurtzite $CuGaS_2$ NCs inhibiting the growth along the ⟨001⟩ direction promoting 2D growth. For example, Adhikari *et al.* demonstrated a non-coordinating solvent in the reaction system formed wurtzite $CuGaS_2$ nano-tadpoles.[51] In contrast, when a coordinating solvent OLA was used, flat 2D nano tadpoles were formed. Similarly, our group observed that using coordinating solvents such as OLA and TOPO in the reaction system for wurtzite $CuIn_{1-x}Ga_x(S_{1-y}Se_y)_2$ synthesis formed nanoplates.[54] However, NCs with intrinsically asymmetric crystal structures such as klockmannite and covellite crystal phases seldom get affected by ligand interaction.[89] In klockmannite, covellite, one $CuE_3$ unit sandwiched between two $CuE_4$ units, comprises a trilayer interconnected to the another trilayer up and down *via* di-chalcogenide bonds along the vertical axis. For such structures, new metal–chalcogenide bond formation can only take place along the linear direction forming 2D NCs.

### 3.2. Effect of alkanethiol and halide anions on copper chalcogenide synthesis

According to Pearson's hard–soft acid–base theory, alkanethiols as soft Lewis bases display a strong affinity towards soft Lewis acidic $Cu^I$ cations. This favourable interaction is responsible for forming columnar or lamellar Cu-thiolate complexes.[48,49,91–93] In the lamellar framework, $Cu^I$ stays confined between hydrophobic layers of alkanethiols.[49] The alkane chain length decides the integrity of the lamellar structure. In the columnar structure, four $Cu^I$ interact with four alkanethiol forming discs that stack with each other.[48] These polymeric complexes can break down above a certain temperature *e.g.*, columnar framework of $Cu^I$-1-DDT breaks down beyond 190 °C. The complexes subsequently undergo an isotropic phase transition to form monomers upon thermolysis of the C–S bond resulting in the isotropic nucleation of pseudospherical NCs. The presence of halide anions can prolong the tenacity of such $Cu^I$-alkanethiolate complexes up to the onset of nucleation.[49,91,94] van der Stam *et al.* observed a $Cu^I$-DDT lamellar structure, which generally melts beyond 150 °C, but remained intact in the presence of chlorides up to 230 °C.[49]

As a result, the nucleation in the 2D lamellar template formed thin nanosheets of $Cu_{2-x}S$ (Fig. 1a and b). It was proposed that the presence of $Cl^-$ as a poly coordinated bridging ligand strengthens the lamellar structure. In another instance, Zhai *et al.* observed the effect of chloride ion on the morphology by varying the ratios between $Cu(NO_3)_2$ and $CuCl_2$ precursors (Fig. 1c).[90] Keeping the total copper precursor concentration constant, a lower concentration of $CuCl_2$ with respect to $Cu(NO_3)_2$ ($CuCl_2/Cu(NO_3)_2$ = 0.53) materialized 1D nanostructures whereas a higher concentration of $CuCl_2$ ($CuCl_2/Cu(NO_3)_2$ = 9) solely formed 2D nanoplates. Similarly, Wu *et al.* varied HCl in a reaction system containing $Cu(OAc)_2$, TOPO, and ODE to see a transition from spherical NPs for zero or low HCl to triangular nanoplates at 2 mmol HCl.[95] Apart from the Cu-halides other metal halides (*e.g.* $SnBr_4$, $SnCl_4$) have also been explored to induce a 2D morphology where their presence instigated 2D templated growth by stabilizing the lamellar complex.[91] Depending on the halide species, the shape of the NCs can be modulated. In the presence of $Br^-$, mostly hexagonal plates or sheets are formed whereas $Cl^-$ predominantly

Open Access Article. Published on 27 January 2022. Downloaded on 11/30/2025 6:59:56 AM.
This article is licensed under a Creative Commons Attribution 3.0 Unported Licence.

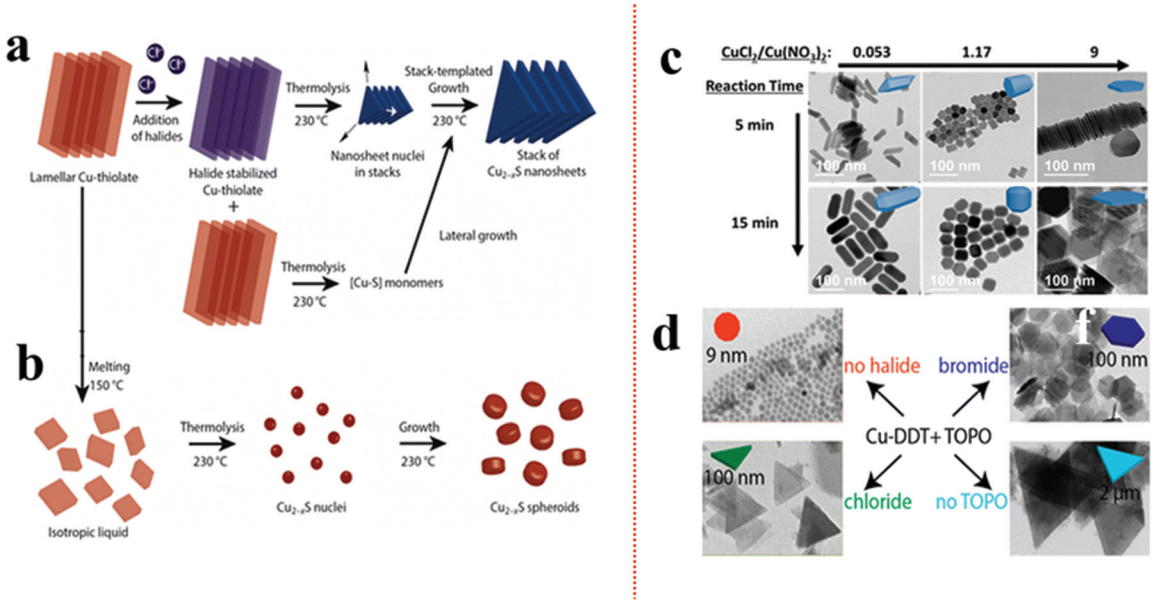


**Fig. 1** (a) Schematic of controlling the 2D shape of the $Cu_{2-x}S$ using $Cl^-$ source. The $Cl^-$ stabilized the lamellar Cu-alkanethiolate structure close to the nucleation stage influencing a 2D templated nucleation; (b) in the absence $Cl^-$ the lamellar structure melts and provides monomers for $Cu_{2-x}S$ nuclei formation resulting in spheroids. Reproduced from ref. 49 with permission from ACS, copyright 2016; (c) effect of ratio variation between $CuCl_2$ and $Cu(NO_3)_2$ on morphology control of $Cu_{2-x}S$. Reproduced from ref. 90 with permission from ACS, copyright 2017; (d) effect of $SnX_4$ (X = Cl, Br) additives on nanoplate formation of $Cu_{2-x}S$. The $Br^-$ source formed hexagonal plates whereas the $Cl^-$ source produced triangular plates. Reproduced from ref. 91 with permission from ACS, copyright 2016.

forms triangular shapes (Fig. 1d).[91,95] In contrast, $I^-$ species which is a soft base does not form any regular shapes. Such disparity can be attributed to the strong interaction between $Cu^+$ and $I^-$, which hampers the formation of Cu-alkanethiolate. However, it is unclear if halide anions can affect the 2D growth of multinary Cu-chalcogenides by forming a soft template as nuclei.

### 3.3. Cation exchange (CE)

The topotactic cationic replacement in 2D $Cu_{2-x}S$ or Se nanoplates are usually used to materialize multi-elemental NCs of different compositions in a two-dimensional morphology.[61,96,98] The high mobility of cations on a rigid anionic lattice is mostly responsible for creating channels for cation replacement.[99] Sequential cationic incorporation in the anionic lattice avoids the unnecessary formation of secondary impurities while keeping the morphology intact. The compositional outcome mostly depends on the following:

(1) Incoming foreign cation valency and its ability to adapt the coordination environment of the template lattice.

(2) The vacancy of Cu cations in the template to facilitate the movement of cations on the rigid anionic lattice.

(3) The presence of mildly reducing soft Lewis base (*e.g.* alkanethiols, tri-alkyl phosphine) to scavenge $Cu^+$ using favourable soft acid–soft base interaction.

$Cu_{2-x}S$ or Se possesses a rich and diverse phase diagram having monosulphide ($Cu_{2-x}S$, $x$ = 0–0.4) and disulphide anions with tetrahedral and trigonal sites. A ternary combination involving a divalent cation ($Cd^{2+}$, $Zn^{2+}$, $Hg^{2+}$ *etc.*) and a monovalent cation cannot satisfy the charge balance in tetrahedral coordination, thus the divalent cations partially or completely replace the Cu cation to form heterostructures or a new binary phase.[36,77] Liu *et al.* outlined the formation of heterostructure nanoplates of $Cu_2S$–CdS on a covellite CuS template by using $Cd^{2+}$ as the foreign cation with 1-DDT. In this study, 1-DDT acted as the $Cu^+$ extractor and reducing agent for CuS to $Cu_2S$ (Fig. 2a).[61] In contrast, trivalent cations such as $In^{3+}$, $Ga^{3+}$ can satisfy the charge balance and alloy to form ternary NCs. Mu *et al.* demonstrated the formation of thin $CuInS_2$ nanoplates using CE of the djurleite $Cu_{2-x}S$ template where $Cu^+$ and $In^{3+}$ share the tetrahedral coordination site.[100] Moreover, with the tetravalent cations ($Sn^{4+}$, $Ge^{4+}$) alloying has also been possible with templates having trigonal sites along with the tetrahedral site. One such example is the cation exchange of CuS nanoplates with $Sn^{4+}$ in the presence of a mild reducing agent, 1-DDT (Fig. 2b).[37] In CuS, two tetrahedral units of the $CuS_4$ sandwich a trigonal $CuS_3$ unit to form a single layer where each layer is connected to the other layer *via* a disulphide bond. Here 1-DDT is crucial to reduce the disulphide bond to expose holes for cation incorporation. Additionally, 1-DDT being a soft base scavenged $Cu^+$ cations to create cation vacancies in the lattice. Upon disulphide bond breakage, $Sn^{4+}$ replaces $Cu^+$ from the trigonal site and keeps the tetrahedral sites intact to form $Cu_2SnS_3$ nanoplates. In contrast, using $Sn^{2+}$ with 1-DDT in the same process generated SnS. However, in the absence of 1-DDT, $Sn^{2+}$ acts as a reducing agent and reduced the disulphide bond in a two-electron reduction process converting all the trigonal sites into tetra-

 This journal is © The Royal Society of Chemistry 2022

Open Access Article. Published on 27 January 2022. Downloaded on 11/30/2025 6:59:56 AM.
This article is licensed under a Creative Commons Attribution 3.0 Unported Licence.

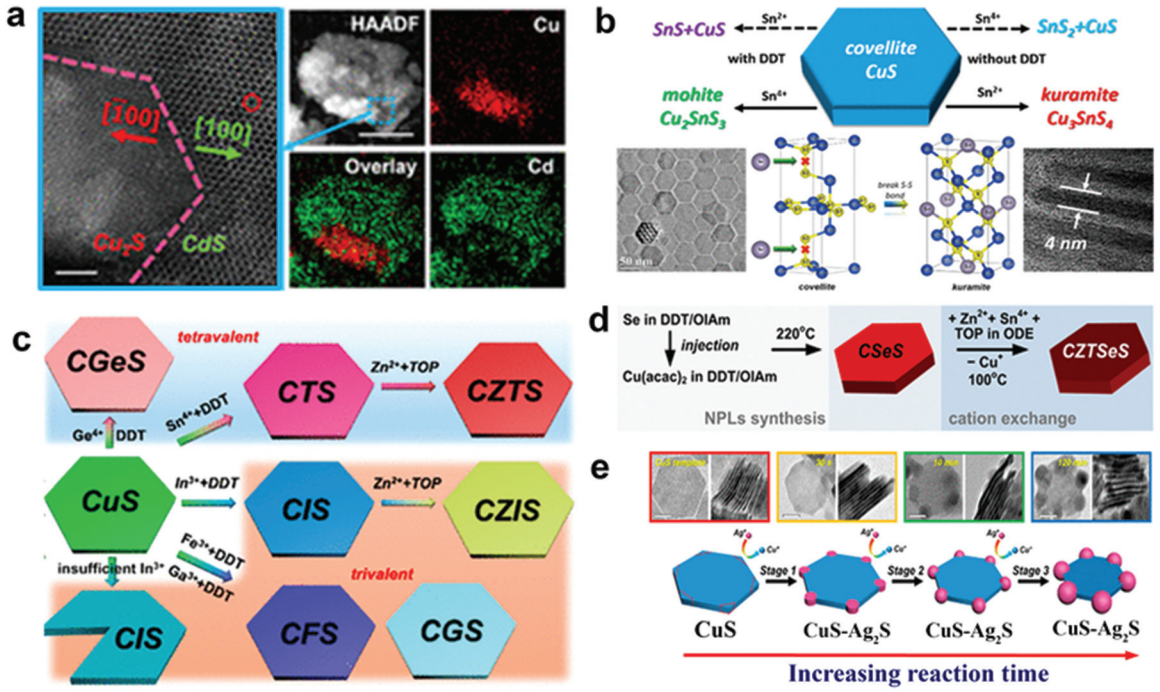


**Fig. 2** (a) CE of the covellite CuS template with $Cd^{2+}$ forming a heterostructure of $Cu_2S$–CdS; reproduced from ref. 61 with permission from ACS, copyright 2018; (b) illustration of outcomes from CE of the covellite CuS template with $Sn^{2+}$ and $Sn^{4+}$ cations in the presence and absence of dodecanethiol as the reducing agent; reproduced from ref. 37 with permission from ACS, copyright 2017; (c) schematic of the CE product from CuS using tri and tetravalent cations. Reproduced from ref. 61 with permission from ACS, copyright 2018; (d) sequential CE of the $Cu_{2-x}Se_ySy_{1-y}$ template forming multi-elemental $Cu_2ZnSnSe_yS_{1-y}$ nanoplates. Reproduced from ref. 96 with permission from ACS, copyright 2014; (e) CE of $Ag^+$ on the CuS template leading to segregated $Ag_2S$ formation at the corners of CuS nanoplates. Reproduced from ref. 97 with permission from ACS, copyright 2018.

hedral co-ordination. Upon the two electron-reduction process of the $Cu_6S_6$ covellite unit, two $Sn^{2+}$ entities convert themselves into $Sn^{4+}$ and incorporate in the tetrahedral sites to form Kuramite $Cu_3SnS_4$ nanoplates. Using 1-DDT as the reducing agent and CuS nanoplates as a template, Liu *et al.* synthesized $Cu_2GeS_3$, $CuInS_2$, $CuGaS_2$, and $CuFeS_2$ nanoplates (Fig. 2c).[61] Once the coordination restriction relaxes upon the introduction of a second cation, divalent cation incorporation is facilitated to form quaternary or multinary nanoplatelets. Lesnyak *et al.* demonstrated the formation of $Cu_2ZnSnSe_yS_{1-y}$ *via* a stepwise cation exchange of $Cu_{2-x}Se_yS_{1-y}$ template using TOP as a soft Lewis base (Fig. 2d).[96] Similarly, the compositions of $Cu_2ZnSnS_4$, $Cu_2ZnGeSe_4$, $Cu_2GeSe_yS_{3-y}$, and $Cu_2ZnGeSe_yS_{4-y}$ were also explored *via* CE.[101,102] Besides providing uniform elemental compositions, CE preserves the anionic sublattice and metal coordination environment in most cases.[103–105] Consequentially, the kinetically trapped phases which are not accessible *via* conventional synthesis approaches could also be materialized. Generally, a template with hexagonal packing of anions will generate the hcp arrangement of anions in the resulting product. This leads to the preferred formation of a wurtzite, monoclinic or rhombohedral crystal phase. Whereas a cubic (ccp, fcc, bcc) packing will result in zinc blende, orthorhombic, and tetragonal crystal phases. For example, using the djurleite $Cu_{1.94}S$ template which possesses a hexagonal S packing, CE with $In^{3+}$ formed wurtzite $CuInS_2$.[57] Similarly, using a digenite $Cu_{2-x}S$ template which possesses cubic close packing (ccp) of S, CE with $In^{3+}$ formed zinc blende $CuInS_2$.[104] Despite having control over the composition and crystal structure of di-, tri-, and tetra-valent cations, the outcome of CE with monovalent cations is less clear.[106–108] Depending on the crystal structure of the template used, the outcome will vary. For example, Swihart and co-workers observed at a lower $Ag^+$ concentration that $Ag_2S$ domains were formed at the corners of the covellite CuS plate when used as a template (Fig. 2e).[97] The high surface energy at the corner lowers the nucleation barrier, due to which most of the CE starts at the corner and gradually reaches the core. The disulphide bond in CuS allowed for the redox reaction and reorganisation that lead to $Ag_2S$ domains to grow further to take a pseudospherical morphology. In contrast, the djurleite $Cu_{1.94}S$ template facilitated the formation of alloyed $Ag_3CuS_2$ plates. In another instance, Kim *et al.* explored the $Cu_{29}S_{16}$ template to materialise segregated $Cu_{31}S_{16}$–$Ag_2S$ plates which evolve into an $Ag_2S$ shell on $Cu_{31}S_{16}$ plates and later again to segregated $Cu_{31}S_{16}$–$Ag_2S$ plates upon Pt shell formation on the basal plane.[109] They suggested the transition of $Cu_{29}S_{16}$ into $Cu_{31}S_{16}$ and strain in $Ag_2S$ facilitated $Ag^+$ migration from the core to shell and again to the core. It is worth mentioning that once the crystal phase reaches a stable structure, exchange of cation ceases. However,

Open Access Article. Published on 27 January 2022. Downloaded on 11/30/2025 6:59:56 AM.
This article is licensed under a Creative Commons Attribution 3.0 Unported Licence.

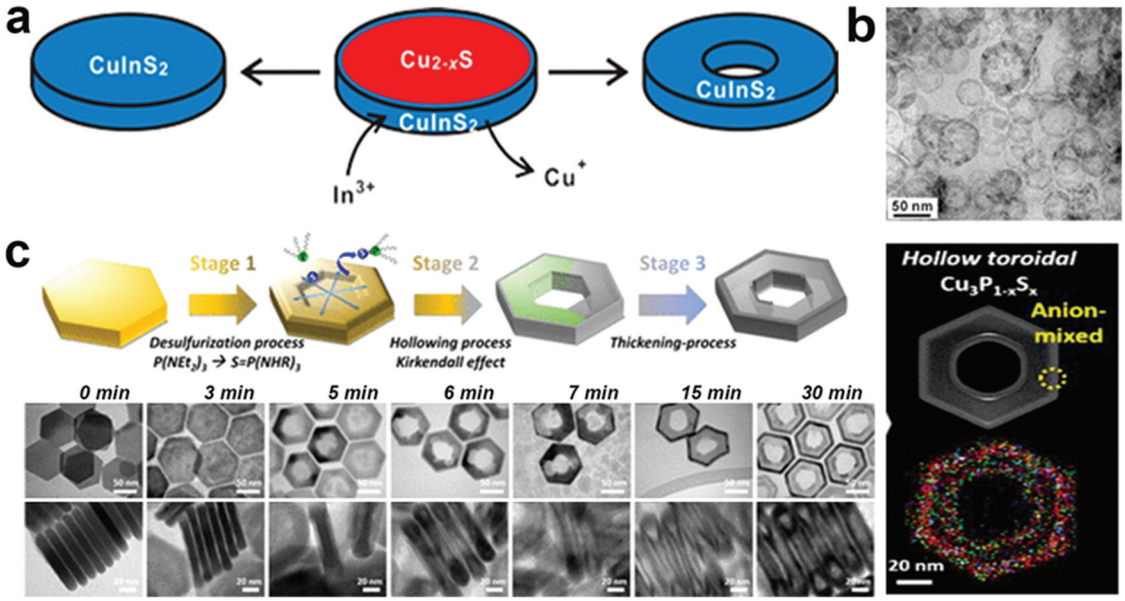


Fig. 3 (a) Illustration of the nanoscale Kirkendall mechanism on the $Cu_{2-x}S$ template for forming (b) hollow $CuInS_2$ nanoplates; reproduced from ref. 110 with permission from ACS, copyright 2015; (c) schematics and low resolution TEM of $Cu_3P_{1-x}S_x$ toroidal ring formation mechanism. The STEM-EDS elemental mapping displays the homogeneous signal of Cu (red), P (green) and S (blue) on the toroidal ring. Reproduced from ref. 64 with permission from ACS, copyright 2020.

high temperature, high lattice strain, and vast difference between the anionic lattice of the template and the desired product can promote reorganisation of the lattice structure and change the shape of the NCs with metastable structures.

In templated cation exchange, variation in the solvation of incoming and outgoing ionic species alters the diffusion rate.[111–113] Due to the difference between diffusion rates of slow incoming foreign cations and fast outgoing host cations, the host cations deplete and form hollow structures in a process called the Kirkendall effect.[111,114] The nanoscale Kirkendall effect is well explored for metal oxide and chalcogenide NCs. For the nanoplate morphologies, when the cation exchange starts from the edges and the outgoing host cation replacement is faster than the incoming ionic species incorporation rate, voids will form in the 2D templates to generate biconcave or toroidal shapes. It is worth mentioning that the nanoscale Kirkendall effect is discernible for a larger template as CE occurs from the edges in an anisotropic template. Hence, the diffusion rate at the basal plane will be significantly different from edges only when the diameter is very large. In $Cu_{2-x}E$ templates, $Cu^+$ is highly mobile; hence, the mobility of the incoming cation will be crucial to control the hollow shape. Mu *et al.* utilized a $Cu_{2-x}S$ template to form perforated $CuInS_2$ plates.[110] The role of $In^{3+}$ was crucial to control the Kirkendall effect (Fig. 3a). They suggested the ability to generate $In^{3+}$ upon nucleophilic attack of $S^{2-}$ varied as $In(OAc)_3 \sim In(acac)_3 > InCl_3 > InI_3$. Thus, the slow release of $In^{3+}$ from $InI_3$ creates a significant difference in the diffusion rate of outgoing fast $Cu^+$ and $S^{2-}$ compared to slower $In^{3+}$ resulting in nanoplates with holes (Fig. 3b). Similarly, Hong *et al.* explored the roxbyte $Cu_{29}S_{16}$ template for a hollowing desulphurisation process using tri(ethyldiamino)phosphine.[64] A Cu migration process occurs following the desulphurisation forming $Cu_3P_{1-x}S_x$ toroidal rings (Fig. 3c). The utilisation of this concept in 2D materials is fairly new, thus opening a window to explore new compositions with hollow 2D morphologies.

## 4. Colloidal synthesis and key growth parameters for 2D morphology

In colloidal synthesis, NC formation proceeds in three stages, (1) decomposition of the precursors and formation of metal anion complexes. (2) Nucleation of monomers; depending on the techniques, the nucleation stage can be either continuous (heat-up) or discrete (hot-injection). For hot-injection, rapid precursor introduction and a temperature gradient between precursor mixtures present in the flask and precursor in the injection induces a supersaturation which leads to a discrete nucleation stage. (3) Growth from monomer deposition on nucleated NCs occurs in two stages where the initial stage is rapid, and the second stage of growth is slow. In the heat-up approach, the first stage of growth and nucleation overlap. In hot injection, the rapid deposition of monomers is essential to terminate nucleation. Here the choice of precursors and ligands is a crucial factor to avoid the formation of secondary phases or to induce the formation of beneficial soft templates. Precursor chemistry can be regulated majorly based on the hard–soft-acid–base theory initially developed by Pearson. Based on the tendency to accept (metal source) or donate electron (ligand), charge on the species, size, and the polarisability

 This journal is © The Royal Society of Chemistry 2022

Open Access Article. Published on 27 January 2022. Downloaded on 11/30/2025 6:59:56 AM. This article is licensed under a Creative Commons Attribution 3.0 Unported Licence.

of the electron cloud, the cations and anions can be categorised as hard, soft and borderline. For example, metal ions with high charge, small size, and low polarisability tend to be hard acids. The anions and cations with a similar nature *i.e.* hard–hard or soft–soft tend to show superior interactions than other combinations, whereas the multifarious role of ligands has been discussed in the previous sections. Another crucial factor is temperature. Modulation of the reaction temperature is a gateway to provide enough energy to control cationic diffusion and crystal phase transition. The following section presents the progress made to synthesise 2D copper-based NCs using colloidal synthesis. We examine their growth process and how certain factors play a vital role in regulating morphologies. The focus is on how various reaction factors such as precursor ratio, ligands classes and their concentration, reaction kinetics, and reaction temperature will alter the 2D morphologies (Table 1). The section is split into Cu chalcogenide and non-chalcogenide based 2D NCs. Copper chalcogenide NCs are further categorized into two sub-sections: binary copper chalcogenides and multinary copper chalcogenides (ternary and quaternary). Furthermore, the section of non-chalcogenide based NCs covers copper phosphides, copper-based alkali metal halides and metal–metal alloys.

### 4.1. 2D copper based chalcogenides

Cu chalcogenides (S, Se and Te) NCs exhibit a wide range of compositions and diverse crystal structures.[40] Therefore, tuning the composition, size and shape is the key to alter their optoelectronic properties for several applications such as thermoelectrics, photovoltaics, catalysis, *etc.* Over the past decade, significant control over the morphology and crystal phases was achieved using colloidal synthesis, including several metastable phases of Cu chalcogenide NCs.[59,133,142,143] This review section will summarize the synthesis advancements in the 2D morphology of binary and multinary *i.e.*, ternary and quaternary NCs.

**4.1.1. Binary copper chalcogenides.** Colloidal binary copper chalcogenide ($Cu_{2-x}E$; E = S, Se, and Te) NCs have gained popularity in recent years due to their unique properties making them suitable for use in various applications. The possibility of multiple compositions and crystal structures can be exploited to tune the size and shape of colloidal $Cu_{2-x}E$ NCs across an extensive range, allowing for multiple morphologies that are not possible with other binary NCs.

P-Type $Cu_{2-x}S$ is the most studied binary copper chalcogenide due to its inherent Cu vacancies. The binary Cu–S system has a very rich phase diagram,[144] with a wide range of equilibrium crystal forms having different 2D morphologies. Copper-rich phases such as chalcocite ($Cu_2S$), djurleite ($Cu_{31}S_{16}$ or $Cu_{1.94}S$), digenite ($Cu_9S_5$ or $Cu_{1.8}S$), and anilite ($Cu_7S_4$ or $Cu_{1.75}S$) usually form as nanoplates or nanodiscs, whereas copper-poor phases including covellite (CuS) and villamaninite ($CuS_2$) exhibit nanosheet-like morphologies. The availability of different S sources provides further accessibility for tuning the size and shape of NCs. For instance, Lesyuk *et al.* employed a hot-injection method to synthesise triangular and hexagonal-like 2D NCs. Altering precursor ratios, reaction temperature, and time resulted in size and shape change (Fig. 4a).[115] They investigated the effect of the Cu : S precursor on the shape of nanostructures. With a high Cu to S precursor ratio, irregular spherical covellite nanodiscs were produced, which progressively transformed into faceted triangles as the Cu : S precursor ratio decreased. The thermodynamic growth mechanism played an important role in the change in morphology. At the start of the reaction with a sufficient supply of sulfur, the most reactive positions (vertex tips) of the triangular NCs were formed, promoting the triangular shape of the initial NCs under kinetic growth. As the reaction proceeds, under equilibrated monomer supply NCs developed with all six facets to minimise the system's surface energy at the expense of smaller triangles, which gradually dissolve to produce hexagonal platelets. Furthermore, the gradual addition of Cu and S precursors into the reaction system formed nanosheets up to 2 microns. In another instance, Du *et al.* materialised CuS nanosheets by reacting sulfur powder and CuCl in the presence of OLA and octylamine at 95 °C for 18 h.[74] The formed nanosheets were found to have an average plane length of 453 ± 6 nm and thickness of 3.2 ± 0.2 nm. The nanosheet formation was attributed to nucleation in a confined lamellar structure due to the reaction of OLA and octylamine with CuCl (Fig. 4b). Gao and co-workers illustrated the formation of Sn-doped ultrathin $Cu_{31}S_{16}$ nanosheets with lateral dimensions >200 nm by varying the quantity of $SnCl_4$ in the reaction medium.[93] The authors proposed that $SnCl_4$ can form stable complexes with dodecanethiol, which acts as surface capping agents, preferentially adhering to the djurleite's (100) facets, resulting in ultrathin 2D nanosheets. Wang *et al.* reported the synthesis of $Cu_2S$ nanodiscs.[116,120] These nanodiscs were formed by injecting 1-dodecanethiol (1-DDT) into a heated solution consisting of copper acetate (CuOAc), tri-octyl phosphine oxide (TOPO), and 1-octadecene (ODE). The rise in injection temperature from 160 to 190 °C increased the size of nanoparticles from 13.1 ± 0.9 nm to 16.9 ± 2.3 nm, whereas monodisperse nanodiscs were obtained with a further increase in temperature to 200 and 220 °C. Xie and co-workers fabricated anisotropic CuS nanodiscs with low size distribution by injecting S–OLA solution in a hot colloidal mixture of CuCl, oleic acid, OLA and 1-ODE.[117] In another study, Li *et al.* revealed that an oriented attachment is critical for the precise control of the size and shape of $Cu_{2x}S$ NCs.[118] At the initial stage of the reaction, $Cu_{2x}S$ spherical nanoparticles were formed by injecting di-*tert*-butyl disulphide (TBDS) into a heated $CuCl_2$ solution. These spherical nanoparticles evolved further into circular nanodiscs and hexagonal $Cu_{1.96}S$ nanodiscs with prolonged reaction times (Fig. 4c). Higher temperatures and longer reaction times enhanced the crystallinity and diameter of the nanodiscs, with minor effects on their thickness, crystallographic phase, and composition. The room temperature synthesis of CuS nanoplates by multiple injections of ammonium sulphide into a mixture of $CuCl_2$, OLA, and toluene was reported by Liu *et al.*[119] The authors achieved

Open Access Article. Published on 27 January 2022. Downloaded on 11/30/2025 6:59:56 AM. This article is licensed under a Creative Commons Attribution 3.0 Unported Licence.

Table 1 Synthesis parameters and crystal structures of 2D copper-based compounds

| Products | Method | Crystal phase | Reactants, ligands, and solvents | Temperature and duration | Ref. |
|---|---|---|---|---|---|
| ***2D-copper-based binary chalcogenides*** | | | | | |
| **Copper sulfide** | | | | | |
| $Cu_xS$ nanoprisms and nanosheets | Hot-injection approach | Hexagonal (covellite) | CuI/CuOAc, S, OLA, S | 120–150 °C/ 30 min | 115 |
| CuS nanosheets | Hot-injection approach | Hexagonal (covellite) | CuCl, S, OLA, octylamine | 95 °C/18 h | 74 |
| Sn doped $Cu_{31}S_{16}$ nanosheets | Heat up approach | Monoclinic djurleite | $Cu(acac)_2$, *n*-dodecanethiol, $SnCl_4{\cdot}5H_2O$ | 200 °C/48 min | 93 |
| $Cu_2S$ nanodiscs | Hot-injection approach | Hexagonal | CuOAc, 1-dodecanethiol (1-DDT), tri-*n*-octylphosphine oxide (TOPO), ODE | 200–220 °C/ 5–540 min | 116 |
| CuS nanodiscs | Hot-injection approach | Hexagonal (covellite) | CuCl, S, OLA, OA, ODE | 180 °C/10 min | 117 |
| $Cu_{2-x}S$ nanodiscs & nanoplates | Hot-injection approach | Monoclinic (roxbyite) | $CuCl_2{\cdot}2H_2O$, di-*tert*-butyl disulfide, OLA | 180–220 °C/ 10–60 min | 118 |
| CuS nanoplates | Hot-injection approach | Hexagonal (covellite) | $CuCl_2{\cdot}2H_2O$, ammonium sulfide, OLA | 200 °C/10 s to 160 min | 119 |
| $Cu_{2-x}S$ nanoplates | Heat up approach | Hexagonal (covellite) | CuCl, S, TOPO, OLA | 85 °C/1 h | 120 |
| **Copper selenide** | | | | | |
| $Cu_{2-x}Se$ nanosheets & nanoplates | Hot-injection approach | Cubic (berzelianite) | CuCl, Se powder, 2-ethylhexanoic acid, OLA, paraffin liquid | 250 °C/30 min | 121 |
| $Cu_{2-x}Se$ & CuSe nanosheets | Hot-injection approach | Cubic/$Cu_{2-x}Se$ hexagonal/CuSe | $CuCl_2{\cdot}2H_2O$, Se powder, hydroxylamine hydrochloride, 1-DDT, OLA | 80 °C/3 h | 122 |
| CuSe nanoplates | Hot-injection approach | Hexagonal | CuCl, Se, OLA, OA, ODE | 300–330 °C/ 15 min | 68 |
| $Cu_{2-x}Se$ nanoplates | Heat up approach | Hexagonal (weissite like) | $Cu(acac)_2$, $Ph_2Se_2$, OLA | 220 °C | 123 |
| $Cu_{2-x}Se$ nanodiscs | Hot-injection approach | Mix phase | CuCl, selenourea, OLA | 200–240 °C/ 10–90 min | 124 |
| $Cu_{2-x}Se$ nanodiscs | Hot-injection approach | Cubic | $CuCl_2$, dimethylimidazoline-2-selenone, OLA, methylene chloride | 175 °C/10 min | 125 |
| **Copper telluride** | | | | | |
| CuTe nanoplates | Hot-injection approach | — | CuCl, TOP–Te, $LiN(SiMe_3)_2$, TOPO, OLA | 190 °C/15 min | 67 |
| $Cu_2Te$ nanodiscs | Hot-injection approach | — | $Cu(acac)_2$, TOP–Te, $C_{12}SH$, OA | 180 °C/2 min | 126 |
| CuTe nanosheets | Heat up approach | — | $Cu(acac)_2$, didodecyl ditelluride, dioctyl ether | 155 °C/1 h | 127 |
| ***2D-copper-based multinary chalcogenides*** | | | | | |
| $Cu_{2-x}S_ySe_{1-y}$ nanodiscs | Hot-injection approach | Monoclinic | CuCl, Se powder, DDT, OLA, ODE | 190 °C/1 h | 128 |
| $CuS_ySe_{1-y}$ nanoplates | Heat up approach | Hexagonal | $Cu(NO_3)_2$, S powder, Se powder, ethanol, NaOH | 80–95 °C/10 h | 129 |
| $CuSbS_2$ rectangular nanosheets | Heat up approach | Orthorhombic | Cu(diethyldithiocarbamate)$_2$, Sb(diethyl-dithiocarbamate)$_3$, OLA, 1-DDT | 220 °C/1 h | 130 |
| $Cu_3SbS_3$ rhombic nanosheets | Heat up approach | Monoclinic | Cu(diethyldithiocarbamate)$_2$(phenanthroline), Sb(diethyldithiocarbamate)$_3$, OLA, 1-DDT | 220 °C/1 h | 130 |
| $CuSbS_2$ nanoplates | Hot-injection approach | Orthorhombic | $Cu(acac)_2$, $SbCl_3{\cdot}6H_2O$, S, OLA | 170–280 °C/ 10–30 min | 22 |
| $CuSbS_2$ nanoplates | Hot-injection approach | Orthorhombic | $Cu(OAc)_2{\cdot}H_2O$, $SbCl_3$, S, OLA | 190 °C/45 min | 55 |
| $Cu_3BiS_3$ nanoplatelets | Hot-injection approach | Orthorhombic | Bi(diethyldithiocarbamate)$_3$, Cu(diethyl-dithiocarbamate)$_2$, OLA, 1DDT | 220 °C/15 min | 56 |
| $CuFeS_2$ nanoplates | Hot-injection approach | Tetragonal | Cu-oleate, Fe-stearate, S, OLA, ODE | 240 °C/1 h | 131 |
| $CuInS_2$ nanodiscs | Heat up approach | Hexagonal | CuCl, $InCl_3$, thiourea, OLA | 240 °C/1 h | 70 |
| $CsCu_5S_3$ nanoplatelets | Hot-injection approach | Orthorhombic | $Cs_2CO_3$, $Cu(acac)_2$, S, OLA, OA | 260 °C/15 min | 65 |
| $Cu_2ZnSnS_4$ nanoplates | Hot-injection approach | Hexagonal wurtzite | $CuCl_2{\cdot}2H_2O$, $SnCl_4{\cdot}5H_2O$, $ZnCl_2$, DDT, OLA, OA | 240 °C/1 h | 132 |
| $Cu_2ZnSnS_4$ nanosheets | Heat-up approach | Hexagonal wurtzite | $Cu(acac)_2$, $Zn(acac)_2$, $SnCl_4{\cdot}5H_2O$, 1-DDT | 250 °C/25 min | 60 |
| $Cu_2ZnSnSe_4$ nanoplates | Hot-injection approach | Hexagonal wurtzite | $Cu(acac)_2$, $Zn(Ac)_2$, $Sn(Ac)_2$, diphenyl diselenide, OLA | 250 °C/15 min | 133 |
| $Cu_2In_xGa_{1-x}(S_ySe_{1-y})_2$ nanoplates | Hot-injection approach | Hexagonal wurtzite | CuI, $In(acac)_3$, $Ga(acac)_3$, diphenyl diselenide, TOPO, 1-DDT, OLA, ODE | 175 °C/25 min | 54 |
| ***2D-copper based non-chalcogenides*** | | | | | |
| **Copper phosphides** | | | | | |
| $Cu_{3-x}P$ nanoplates | Hot-injection approach | Hexagonal | Cu NCs solution, TOP, TOPO, OLA | 320 °C/1 h | 69 |
| $Cu_3P$ nanoplates | Heat-up approach | Hexagonal | CuCl, TOP, TOPO, octylamine, OLA | 350 °C/10 s to 25 min | 23 |
| $Cu_3P$ nanoplatelets | Heat up approach | Hexagonal | CuCl, $PH_3$ gas TOP, TOPO, octylamine, OLA | 200–230 °C/ 15 min | 134 |
| $Cu_{3-x}P$ nanodiscs | Hot-injection approach | Hexagonal | CuCl, $(TMS)_3P$, TOP, OLA, ODE | 300 °C/10 min | 50 |
| $Cu_{3-x}P$ nanodiscs | Heat up approach | Hexagonal | $CuCl_2$, triphenyl phosphite, hexadecylamine, ODE, EtOH | 300 °C | 135 |
| $Cu_{3-x}P$ nanoplates | Heat up approach | Hexagonal | CuCl, $P(NEt_2)_3$, OLA, ODE, trioctylamine | $T_f \approx 280$ °C | 136 |


This journal is © The Royal Society of Chemistry 2022

Open Access Article. Published on 27 January 2022. Downloaded on 11/30/2025 6:59:56 AM.
This article is licensed under a Creative Commons Attribution 3.0 Unported Licence.

Table 1 *(Contd.)*

| Products | Method | Crystal phase | Reactants, ligands, and solvents | Temperature and duration | Ref. |
|---|---|---|---|---|---|
| **Ternary Cu-based halides** | | | | | |
| $Cs_3Cu_2I_5$ nanodiscs | Hot-injection approach | Orthorhombic | CuI, Cs-oleate, OLA, ODE, OA | 70–80 °C/30 s | 34 |
| $Cs_3Cu_2Br_5$ nanoplates | Hot-injection approach | Orthorhombic | CuBr, Cs-oleate, OLA, ODE, OA | 70–80 °C/30 s | 34 |
| $Cs_3Cu_2I_5$ nanoplates | Hot-injection approach | Orthorhombic | CuI, Cs-oleate, OLA, ODE, OA | 110 °C/10 s | 62 |
| $Cs_3Cu_2Br_5$ nanoplates & nanodiscs | Hot-injection approach | Orthorhombic | CuBr, Cs-carboxylate, ODE, {(hexanoic acid/ nonylamine) for nanoplates}, {(nonanoic acid/ OLA) for nanodiscs} | 70 °C/25 s | 137 |
| $Rb_2CuX_3$ (X = Cl, Br) | Mix-up approach | Orthorhombic | RbX (X = Cl, Br), CuX (X = Cl, Br), DMSO, OA, toluene | Room temperature | 33 |
| **Metallic Cu-based NCs** | | | | | |
| Cu nanoplate | Heat up approach | Cubic | $CuSO_4{\cdot}5H_2O$, ascorbic acid, CTAB, NaOH, water | 85 °C/2.5 h | 138 |
| Cu nanosheet | Heat up approach | Cubic | $Cu(NO_3)_2{\cdot}3H_2O$, ascorbic acid, CTAB, hexamethyl-enetetramine, water | 80 °C/3 h | 139 |
| Cu nanoplate | Heat up approach | Cubic | $Cu(OAc)_2{\cdot}H_2O$, poly(vinyl pyrrolidone), DMF, hydrazine, water | 60 °C/3–4 min | 140 |
| Cu nanoplate | Heat up approach | Cubic | $CuBr_2$, ascorbic acid, branched polyethyleneimine water | 90 °C/10 h | 88 |
| Ni–Cu alloy nanoplates | Heat up approach | Defected cubic | $CuCl_2{\cdot}2H_2O$, $Ni(acac)_2$, OLA, TOP, dibenzyl ether | 175–240 °C/1 h | 24 |
| PdCu alloy nanosheets | Heat up approach | Cubic | $Cu(acac)_2$, $Pd(acac)_2$, $Mo(CO)_6$, TOPO, DMF, OA | 60 °C/18 h | 85 |
| Cu–Ag alloy NCs | Heat up approach | Cubic | $Cu(acac)_2$, Ag(Ac), OLA, OA, ODE | 180 °C/30 min | 141 |

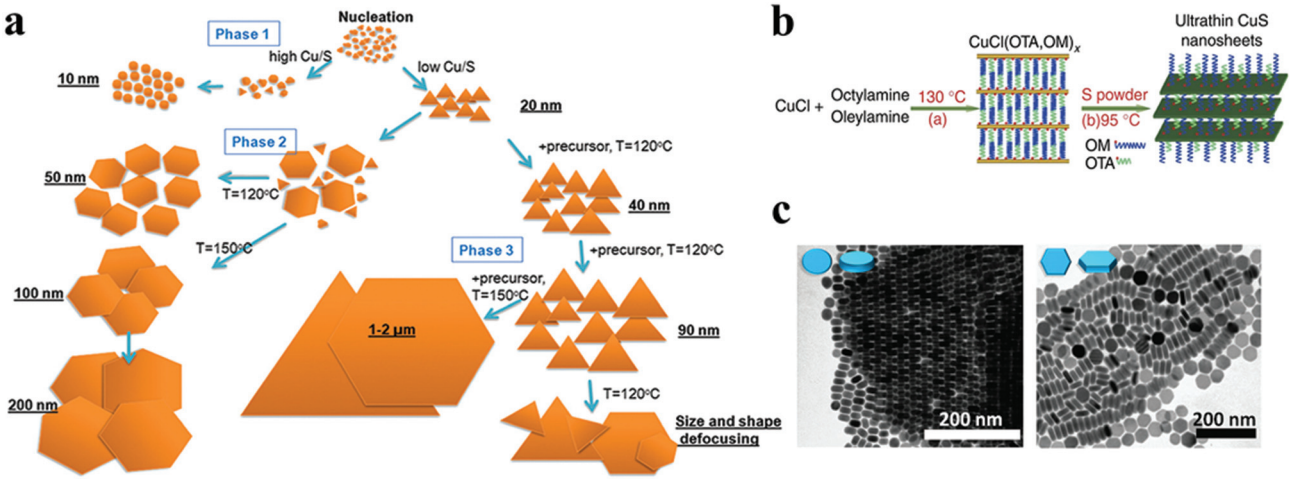


Fig. 4 (a) The shape transformations during the OAm–S based hot-injection copper sulphide synthesis are shown in a scheme, along with methods to control the shape. Reproduced from ref. 115 with permission from RSC, copyright 2018; (b) schematic illustration of fabrication of ultrathin CuS nanosheets.[74] ©2012 Nature (c) TEM images showing the morphology evolution of $Cu_{2-x}S$ NCs. Reproduced from ref. 118 with permission from RSC, copyright 2011 ©2011 RSC.

a wide variety of NC sizes by varying the number of ammonium sulphide injections, ranging from large nanosheets to smaller nanoparticles. A single ammonium sulphide injection resulted in large irregularly shaped plates with high polydispersity. A series of smaller injections with an overall constant volume of ammonium sulphide solution resulted in NCs with decreased average size and low polydispersity. Heating the copper precursor and sulfur powder demonstrated a simple synthesis protocol for the formation of monodisperse $Cu_{2-x}S$ nanoplates at 85 °C in a solution containing OLA and TOPO.[120]

Copper selenide is another notable p-type binary semiconductor with potential uses in solar cells, thermoelectric converters, solar cells, photothermal treatment, and photocatalytic activity.[41,123] Copper selenide has a range of crystal structures dictated by stoichiometric and non-stoichiometric phases. It exhibits a variety of phases, ranging from Cu-deficient hexagonal klockmannite CuSe to copper-rich bellidoite cubic $Cu_2Se$. There are few reports on 2-D copper selenide among the various 2-D nanostructures of metal chalcogenides. Deng *et al.* synthesised berzelianite $Cu_{2-x}Se$ nanoplates and nanosheets by injecting Cu(I)-complex precursor solution into a hot reaction mixture of selenium powder and paraffin oil.[121] Higher copper concentrations resulted in nanosheets with diameters of 1.0–2.5 μm, whereas lower copper concentrations resulted in nanoplates. In the case of

Open Access Article. Published on 27 January 2022. Downloaded on 11/30/2025 6:59:56 AM.
This article is licensed under a Creative Commons Attribution 3.0 Unported Licence.

lower copper content, the facets of the NCs are likely to be extensively passivated, resulting in a reduced in-plane diameter. Another study reported the formation of cubic $Cu_{2-x}Se$ nanosheets *via* simply heating micro-sized CuSe nanosheets in the presence of Cu(I) cations without any morphological modification.[122] The authors proposed that the structure of klockmannite CuSe, which has a low Cu cation occupancy, functioned as a suitable template for additional Cu cation insertion, which led to the formation of antifluorite $Cu_{2-x}Se$ (Fig. 5a). Different selenium sources have been reported to synthesise 2D $Cu_{2-x}Se$ NCs with morphologies like disc and plates. For instance, Deka and co-workers reported a hot-injection approach to fabricate stoichiometric CuSe hexagonal nanoplatelets using Se–ODE solution as a Se source.[68] Injecting Se–ODE solution into a colloidal solution of CuCl in OLA and ODE formed nanoplatelets with dimensions of over 100 nm. Alternatively, selenourea has been employed as a Se source in a hot injection synthesis derived nanodisc with a diameter of 16 nm.[49] Furthermore, a diaryldichalogenide precursor, diphenyl diselenide, directed the synthesis of hexagonal nanoplates of copper selenide.[123] In a seminal work, an air-stable selenium source, namely 1,3-dimethylimidazoline-2-selenon has been synthesised and employed for the hot-injection synthesis of $Cu_{2x}Se$ nanodiscs.[125] The authors suggested that the N-heterocyclic carbenes formed from imidazoline-2-selenone and oleylamine worked together to form nanodiscs by interacting with copper on a crystal plane (Fig. 5b).

Similar to $Cu_{2-x}S$, $Cu_{2-x}Te$ exhibits Cu-deficiency-dependent plasmonic behaviour, high ionic conductivity, and low thermal conductivity and finds applications in photothermal therapy, surface-enhanced Raman scattering probes, and thermoelectric devices.[31,145,146] $Cu_{2-x}Te$ possesses a complex

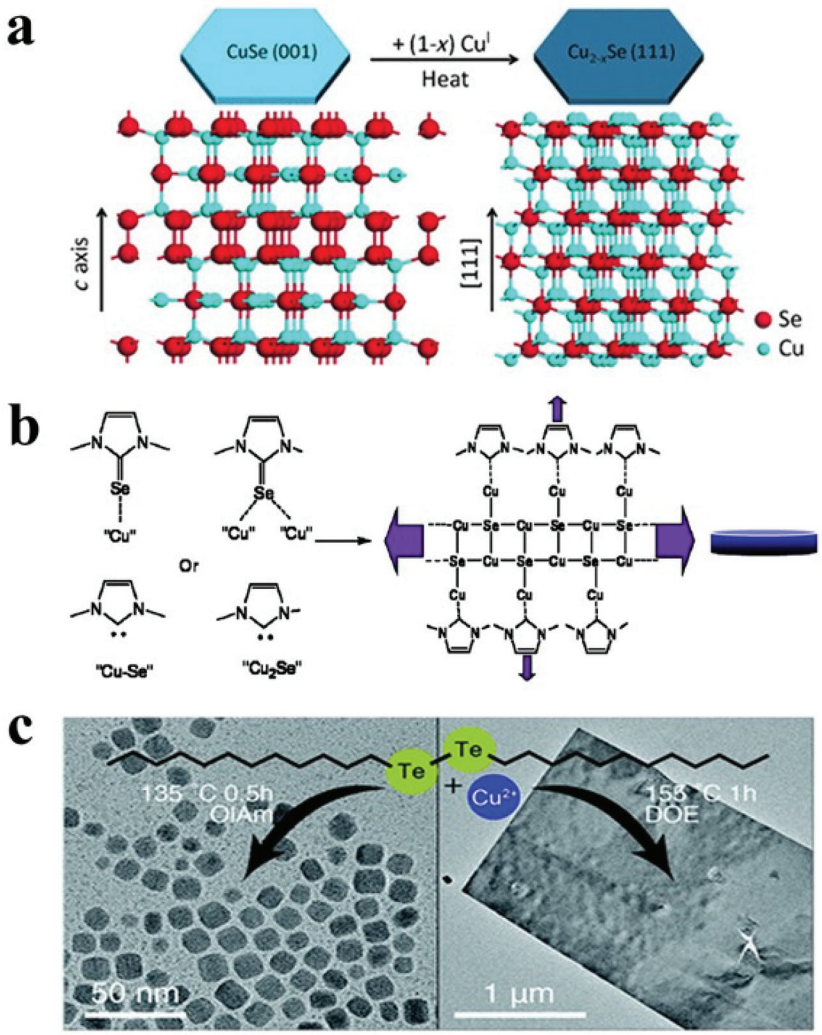


**Fig. 5** (a) Schematic illustrating transformation from hexagonal CuSe to cubic $Cu_{2-x}Se$ under heat treatment due to insertion of CuI; reproduced from ref. 122 with permission from Wiley, copyright 2014; (b) mechanism of cubic $Cu_{2-x}Se$ nanodisc formation *via* imidazoline-2-selenone interaction with NC surface; reproduced from ref. 125 with permission from ACS, copyright 2010; (c) formation of $Cu_{2-x}Te$ NCs and vulcanite nanosheets under different reaction condition using di-dodecyl ditelluride as the Te precursor. Reproduced from ref. 127 with permission from RSC, copyright 2020.

 This journal is © The Royal Society of Chemistry 2022

Open Access Article. Published on 27 January 2022. Downloaded on 11/30/2025 6:59:56 AM.
This article is licensed under a Creative Commons Attribution 3.0 Unported Licence.

phase diagram with many stoichiometries and crystal structures. For example, $Cu_2Te$ (hexagonal), $Cu_7Te_4$ (trigonal), $Cu_3Te_2$ (tetragonal), and CuTe (orthorhombic) are a few notable members of this family. Controlling the 2D shape of the $Cu_{2-x}Te$ NCs remains challenging due to the limited Te precursor availability. Li *et al.* utilized tri-octyl phosphine (TOP)–Te as the Te source with lithium bis(trimethylsilyl) amide and CuCl in the presence of OLA and TOPO to materialize rectangular $Cu_{2-x}Te$ nanoplates at 190 °C.[67] Lithium bis (trimethylsilyl)amide was suggested to activate the Cu-oleylamido complex responsible for $Cu_{2-x}Te$ formation. In another approach, Li *et al.* synthesized hexagonal $Cu_{2-x}Te$ nanoplates by injecting TOP–Te solution in a hot colloidal mixture of $Cu(acac)_2$, 1-DDT and OLA.[126] Switching to a longer chain length thiol (octadecanethiol) led to the formation of nanodots suggesting the suppression of growth for $Cu_{2-x}Te$ NCs. Robinson *et al.* used di-dodecyl ditelluride as the Te source to synthesise vulcanite CuTe nanosheets in dioctyl ether (DOE) at 155 °C for 30 min to 1 h.[127] A low temperature of 135 °C and co-ordinating solvents such as OLA and OA produced $Cu_{1.5}Te$ NCs. In contrast, using DOE at an elevated temperature of 155 °C formed nanosheets predominantly (Fig. 5c).

**4.1.2. Multinary copper chalcogenides.** Changing the composition of binary copper chalcogenide NCs to multinary by the substitution of cations or anions modulates the optoelectronic and chemical properties of NCs such as the alteration of band gap and majority charge carrier concentration and change in the crystal phase, which are interesting for several technological developments.[40,106] For example, in Cu-based chalcogenides, Se substitution in a S-rich crystal lattice enables efficient band gap tuning and renders the plasmonic behaviour in the NIR range,[147] whereas metal substitution can alter the behaviour of majority charge carriers. This added advantage also comes with the complexity of funneling the reactivity of those cation and anionic species to a level that prevents any binary impurity formation. More often, the multinary Cu-chalcogenide NC formation starts with $Cu_{2-x}S$ or Se nuclei formation. The cation or anions present in solution sequentially substitute into the ion-conducting $Cu_{2-x}S$/Se lattice to form multinary NCs. Besides the added advantage of enhanced properties for multinary NCs, the complexities associated with side reactions are always a concern. Hence, choosing the appropriate reaction parameters such as solvent composition, temperature window, and ligands based on the reactivity of the cationic and anionic precursors is crucial to obtain phase pure NCs. The hot-injection system has been effective for multinary metal chalcogenide NC formation as the nucleation events can be judiciously synchronised to avoid binary phase formation. For instance, the addition of a high concentration of 1-DDT (S precursor and coordinating ligand) with respect to Se–ODE solution transformed the cubic berzelianite structure of $Cu_{2-x}Se$ to a monoclinic $Cu_{2-x}S_ySe_{1-y}$ structure with a hexagonal chalcogenide sublattice accompanying a shape change of triangular $Cu_{2-x}Se$ NCs to $Cu_{2-x}S_ySe_{1-y}$ disc shaped nanoplates (Fig. 6a and b).[128] Xu *et al.* showcased an aqueous medium based procedure where $Cu(NO_3)_2$ solution was injected into an alkaline S–Se mixture to form hexagonal $CuS_ySe_{1-y}$ nanoplates. Heating the aqueous solution of the $CuS_ySe_{1-y}$ NCs at 100 °C transformed the hexagonal $CuS_ySe_{1-y}$ completely to face-centered cubic $Cu_{2-x}S_ySe_{1-y}$ after 10 h.[129] The pnictogen (*e.g.*, Sb, Bi) incorporation to form ternary colloidal copper based chalcogenide (I–V–VI) 2D NCs has also been achieved using hot-injection and heat-up setups. Xu *et al.* reported a single source precursor-based reaction using Sb(di-

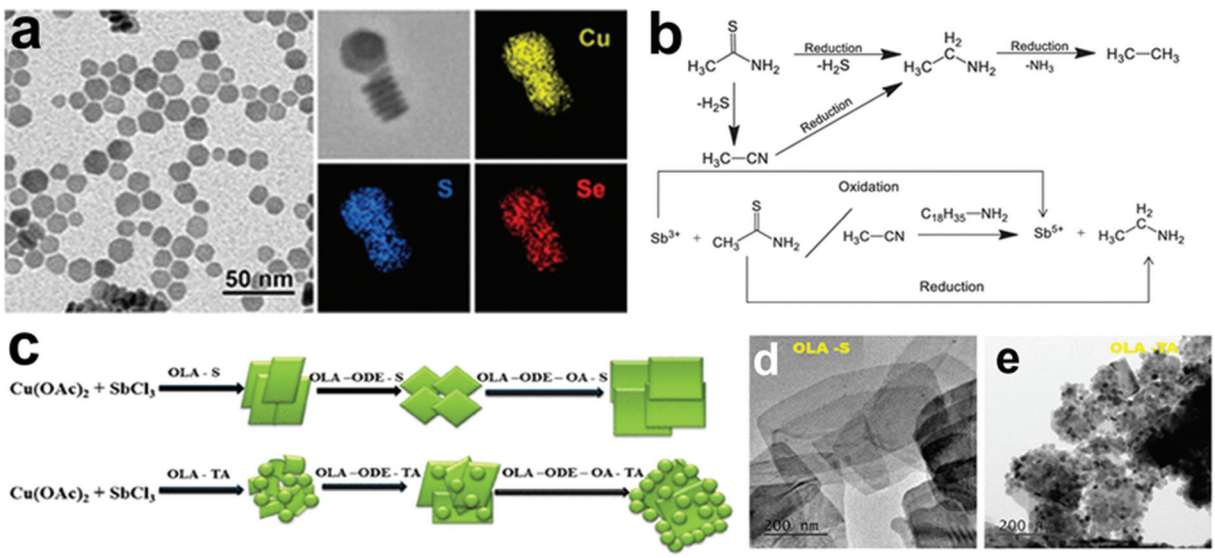


**Fig. 6** (a) TEM image and EDS elemental mapping of $Cu_{2-x}SySe_{1-y}$ NCs synthesized in the presence of 5 mL of 1-DDT; reproduced from ref. 128 with permission from ACS, copyright 2017; (b) schematic showing reduction thioacetamide and oxidation of $Sb^{3+}$ to $Sb^{5+}$, (c) reaction scheme for the formation of (d) $CuSbS_2$ nanoplates and (e) the $CuSbS_2$–$Cu_3SbS_4$ composite using S–OLA and thioacetamide respectively. Reproduced from ref. 55 with permission from ACS, copyright 2019.

Open Access Article. Published on 27 January 2022. Downloaded on 11/30/2025 6:59:56 AM.
This article is licensed under a Creative Commons Attribution 3.0 Unported Licence.

ethyldithiocarbamate)$_3$ and Cu(diethyldithiocarbamate)$_2$ in OLA to synthesize rectangular orthorhombic $CuSbS_2$ nanosheets.[130] Upon modulation of Cu precursor reactivity by using Cu(diethyldithiocarbamate)$_2$(phenanthroline) and diluting OLA using 1-DDT as a co-solvent resulted in rhombic $Cu_3SbS_3$ nanosheets. The authors suggested the dilution of OLA prevented (001) facet specific binding beneficial for growth along the less passivated ⟨111⟩ direction. Additionally, the presence of phenanthroline as a chelating ligand further inhibited growth along subsequent facets forming a rhombic shape instead of a rectangular shape. Ramasamy *et al.* used a hot injection procedure using S–OLA solution with Cu(acac)$_2$ and $SbCl_3$ as cation sources to form multilayer $CuSbS_2$ nanoplates with a minimum of 6 layers stacked along the ⟨001⟩ direction,[22] whereas changing the anionic precursor source to a mixture of thiols 1-DDT and *tert*-DDT formed thick mesobelts of $CuSbS_2$. Behera *et al.* reported $CuSbS_2$ nanoplate synthesis using a similar method of injecting S–OLA solution into Cu(OAc)$_2$ and $SbCl_3$ (Fig. 6d and e).[55] However, changing the S-source to thioacetamide produced nanocomposites of $Cu_3SbS_4$ particles on $CuSbS_2$ nanoplates (Fig. 6d and e). The thioacetamide decomposed to $H_2S$ and acetonitrile ($CH_3CN$). $H_2S$ acted as an active S source, and the acetonitrile got reduced to $CH_3NH_2$ by $Sb^{3+}$ forming $Sb^{5+}$ (Fig. 6c). As a result, both $Sb^{3+}$ and $Sb^{5+}$ species became available in the reaction mixture forming nanocomposites of $Cu_3SbS_4$–$CuSbS_2$.

Bera *et al.* reported the formation of $Cu_3BiS_3$ nanoplatelets by using single source precursors, Bi(diethyldithiocarbamate)$_3$ and Cu(diethyldithiocarbamate)$_2$ decomposition in OLA.[56] The shape of the NCs was controlled either by adding both metal sources together in the flask or by adding a small quantity of the Cu source in the flask ahead of the Cu and Bi-source mixture injection(Fig. 7b). The shape of the platelets was determined by the local concentration of the $Cu_7S_4$ NCs formed initially around the $Cu_3BiS_3$ NCs to go through a ripening process (Fig. 7a and b). Conditions that favoured the high concentration of $Cu_7S_4$ NCs near the $Cu_3BiS_3$ nucleation sphere formed flat and longer nanoplatelets. For example, a high amount of the Cu-source in the first addition, high temperature, and lower solvent volume resulted in the formation of $Cu_7S_4$ NCs in high numbers facilitating the ripening of $Cu_3BiS_3$ NCs to form flat nanoplatelets, whereas a low amount of the Cu-source in the first addition, lower temperature, and a high volume of solvent resulted in the formation of $Cu_7S_4$ NCs in a low number, hence obtaining tapered nanoplatelets (Fig. 7c).

Among other tri-valent cations, $Fe^{3+}$ and $In^{3+}$ have also been explored to form ternary Cu-chalcogenide based 2D NCs.[21,53,70,131] For example, Gabka *et al.* injected S–OLA solution into a Cu-oleate and Fe-stearate mixture present in ODE to materialize $CuFeS_2$ nanoplates.[131] In another work, $CuInS_2$ nanodiscs were synthesized using a heat-up approach where CuCl, $InCl_3$, and thiourea in OLA were heated up to 240 °C for 1 h.[70] Due to the low energy difference between the wurtzite and cubic phase of $CuInS_2$ (~0.1 eV per atom), polytypism was observed along the *c*-axis of these nanodiscs. Berends *et al.* prepared In-poor Cu–In–S nanosheets *via* self-organisation of pre-formed trigonal pyramidal shaped cubic $CuInS_2$ in alkylamine and S–ODE solution (Fig. 8a–d).[21] The reactive sulphur species, generated *in situ via* the reaction of alkylamine and elemental sulphur, extracted $In^{3+}$ cations to form In-poor CuInS NCs. These In-poor NCs underwent oriented attachment

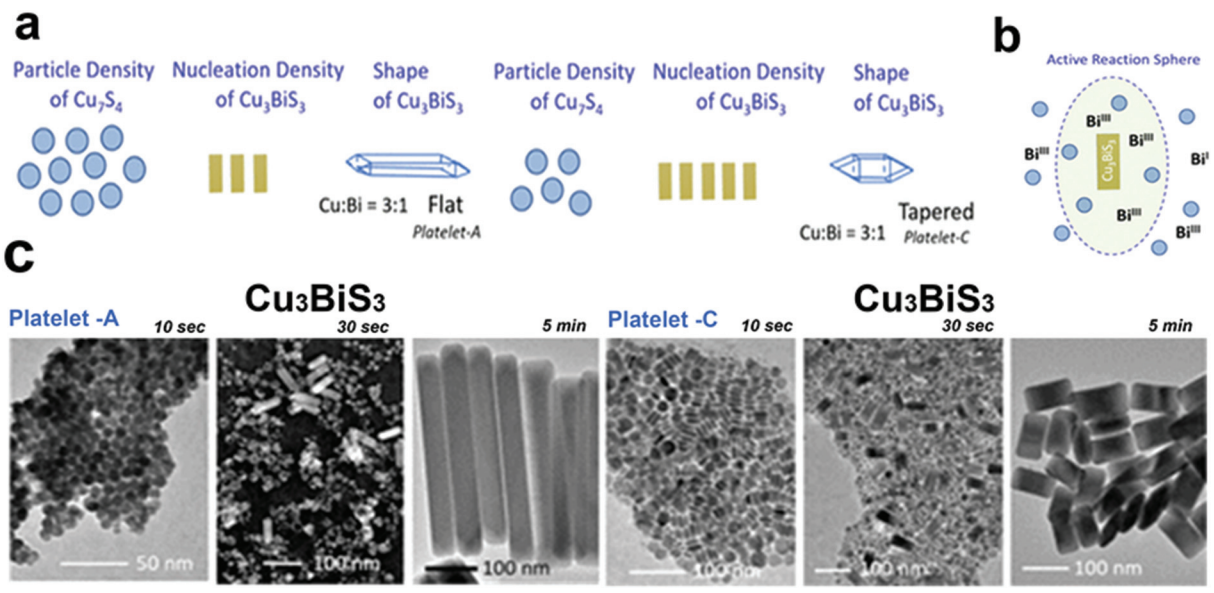


Fig. 7 (a) Schematic presentation of the number density variation reactions of $Cu_7S_4$ and $Cu_3BiS_3$ ternary nuclei forming flat platelets for high number density of $Cu_7S_4$ nuclei and tapered platelets for low number density of $Cu_7S_4$ (b) the active reaction sphere model showing the growth of $Cu_3BiS_3$ nanoplatelets in the presence of Bi(III) precursor and $Cu_7S_4$ platelets, (c) TEM images for the formation pathways collected at different growth times of flat and tapered $Cu_3BiS_3$ nanoplatelets. Reproduced from ref. 56 with permission from ACS, copyright 2020.


This journal is © The Royal Society of Chemistry 2022

Open Access Article. Published on 27 January 2022. Downloaded on 11/30/2025 6:59:56 AM.
This article is licensed under a Creative Commons Attribution 3.0 Unported Licence.

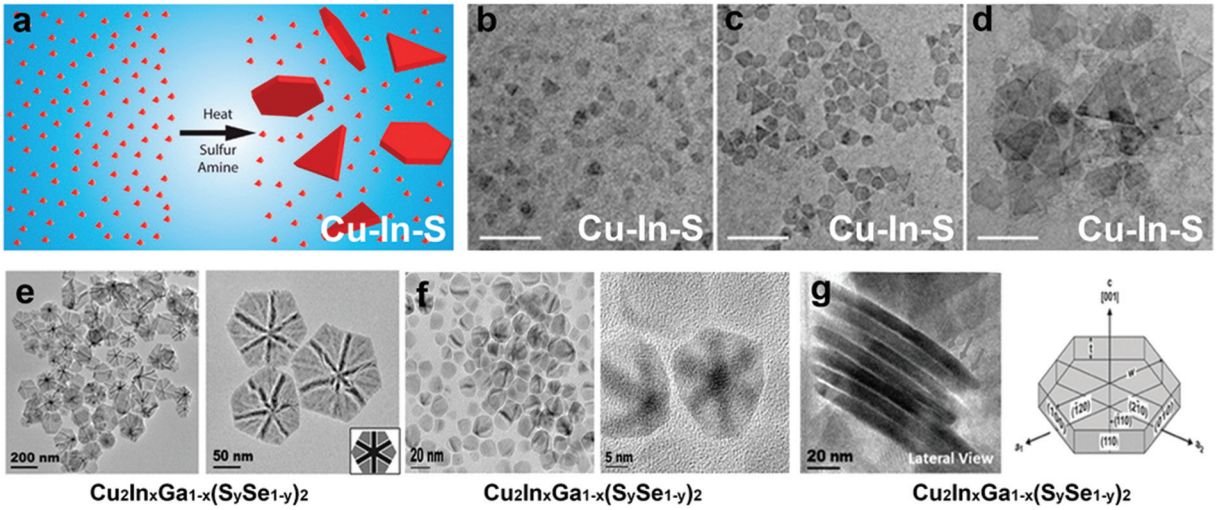


Fig. 8 (a) Schematic representation of the formation of Cu–In–S nanosheets generated *via* oriented attachment of $CuInS_2$ nanopyramids, TEM image depicting the evolution of the nanosheets collected after (b) 1 min, (c) 2 min (d) 5 min; Reproduced from ref. 21 with permission from ACS, copyright 2017; (e) TEM image of the $Cu_2In_xGa_{1-x}(S_ySe_{1-y})_2$ disc with bend contours synthesised using TOPO as the coordinating solvent, (f) TEM image of the $Cu_2In_xGa_{1-x}(S_ySe_{1-y})_2$ disc with shallow bend contours synthesised using TOPO and OLA as the solvent, (g) TEM image showing lateral view of the nanodisc where the cartoon depicts the prismatic and basal planes. Reproduced from ref. 54 with permission from ACS, copyright 2018.

to minimize their surface energy and form hexagonal In-poor CuInS nanosheets with lateral dimensions of 20 nm to 1 μm with a thickness of ~3 nm (Fig. 8a). Among other compositions, Yang *et al.* reported colloidal hexagonal $CsCu_5S_3$ nanoplatelets with a narrow size distribution of 32.3 ± 4.3 nm *via* a hot injection method.[65] To obtain nanoplatelets, S–OLA solution was injected as a chalcogenide source into the mix of Cs-carbonate and Cu-acetate precursors at 260 °C. The synthesised NCs showed an orthorhombic structure with a direct bandgap of 1.40 eV. Quaternary $Cu_2ZnSnS_4$ nanoplates were prepared using the injection of metal thiolates in a solution mixture of 1-DDT and oleic acid.[132] Using a heat up approach, Zhang *et al.* prepared $Cu_2ZnSnS_4$ nanosheets in the wurtzite phase with lateral dimensions of 350 ± 50 nm and a thickness of ~5 nm.[60] In this work, the metal precursors were mixed with 1-DDT and heated to 250 °C. Upon heating $Cu_{2-x}S$ nuclei formed around 220 °C, which transformed into $Cu_2ZnSnS_4$ nanosheets gradually. Ren *et al.* used a dual injection process in which $Sn(OAc)_2$, diphenyldiselenide, and OLA were used as the first injection mixture, and $Zn(OAc)_2$ and OLA as the second injection mixture to synthesize wurtzite $Cu_2ZnSnSe_4$ nanoplates.[133] The double injection procedure ensured the segregation of Cu and Se nucleation with the rest of the cations and made room for uninterrupted sequential incorporation of Sn and Zn. Coughlan *et al.* synthesized curved $Cu_2In_xGa_{1-x}(S_ySe_{1-y})_2$ with contours using TOPO as the co-ordinating solvent (Fig. 8e).[54] The use of a coordinating ligand was determined to be necessary to synthesize metastable wurtzite nanoplates. As the prismatic planes of the nanoplates are nonpolar, the specific binding of TOPO to metal rich basal (001) facets influenced a higher growth rate on the prismatic planes compared to the well-passivated basal planes forming the contours. However, replacing TOPO with another co-ordinating solvent *i.e.*, OLA generated nanoplates without contours, and using a combination of both OLA and TOPO generated nanoplates with shallow curves (Fig. 8f). It was hypothesised that the linear branch of OLA passivates flat surfaces, whereas the bulky TOPO preferred binding to curved surfaces (Fig. 8g).

Nevertheless, there are some challenges regarding the synthesis of colloidal Cu chalcogenide NCs, particularly in the case of selenides and tellurides, for which there are limited anion precursors. The alternative can be the more convenient alkahest solutions of Se and Te and di-orgnyl Se and Te precursors.[47,148] Soft-templated growth is a crucial way to achieve ultrathin NCs. However, the multinary Cu chalcogenide NCs with ultrathin thickness are difficult to materialise from the existing soft-template regimes used for 2D nanostructure formation which degrades typically at higher temperatures (>220 °C), restricting the uniform incorporation of elements in the synthesised NCs. A viable approach will be to employ a double injection approach where the initial injection will ensure the formation of a soft template, and second injection just after the Cu–S bond formation will ensure the diffusion of cations into the pre-nucleated template to form multinary compositions. Another approach could be to design heterometallic single-source precursors which can provide a 2D template during metal–sulfide bond formation.[149]

### 4.2. Cu based non-chalcogenides

Besides copper chalcogenides, there are few examples of 2D anisotropic copper NCs. Copper phosphide ($Cu_{3-x}P$), alkali metal copper halide, and copper-based alloys are some NCs that have shown 2D anisotropic shapes in colloidal synthesis. This section describes the key synthesis insights from recent reports on 2D Cu-based non-chalcogenide NCs.

Open Access Article. Published on 27 January 2022. Downloaded on 11/30/2025 6:59:56 AM.
This article is licensed under a Creative Commons Attribution 3.0 Unported Licence.

**4.2.1. Copper phosphide.** $Cu_{3-x}P$ covers a wide range of applications, from battery anodes to photovoltaic absorbers and from supercapacitors to photo and electrocatalysts. $Cu_{3-x}P$ possesses a hexagonal crystal structure and belongs to the *P*63*cm* space group. The unit cell of bulk $Cu_{3-x}P$ has four distinct Cu sites and one P site. Two of the four different copper sites produce two planar layers stacked to form a hexagonal model with triangular prism voids. The remaining two distinct copper atoms are inserted alternately in these voids.[150] $Cu_{3-x}P$ nanoparticles are typically single domain crystals, and their morphology tends to be characterised by hexagonal facets derived from their hexagonal crystal structure (Fig. 9a). Henkes *et al.* demonstrated the first colloidal method for producing size-controlled and colloidally stable $Cu_{3-x}P$ nanoplates.[69] Here, TOP was used as a phosphorous source. In the first stage of the synthesis, Cu metallic nanoparticles were produced. Subsequently, these metallic nanoparticles were phosphorised with no change in their size and shape, yielding $Cu_{3-x}P$ NCs with a narrow size distribution. De Trizio *et al.* reported a detailed study of two "one-pot" approaches to synthesise hexagonal colloidal $Cu_{3-x}P$ NCs.[23] A comprehensive mechanistic perspective of how the Cu nanocrystal phosphorised over time to $Cu_{3-x}P$ in terms of morphology was demonstrated. The synthetic approach was similar to Henkes *et al.* In this approach, dimeric Janus-like nanoparticles were formed as intermediates, with two domains consisting of Cu and $Cu_{3-x}P$ and sharing a flat epitaxial interface (Fig. 9b). These morphologies indicated that phosphorisation most likely began with the formation of a small $Cu_{3-x}P$ domain on the surface of Cu NCs initially and then proceeded progressively from that region across the whole NC. The authors observed that the inhomogeneous surfactant coverage on the surface of NCs would have prevented the phosphorisation process from progressing in a centrosymmetric way, leading to nanoplates instead of the Cu@$Cu_{3-x}P$ core–shell morphology. The other approach involves directly nucleating plate-like $Cu_{3-x}P$ NCs with a hexagonal structure, which transformed to 2D nanoplates (~50 nm) at 350 °C, over 30 min. $Cu_{3-x}P$ NCs were observed when a TOP : Cu molar ratio of at least 11 : 1 was used, with no apparent intermediary formation of Cu NCs. Furthermore, increasing the amount of TOP causes particles to become more polydisperse and more prominent in size, primarily due to Ostwald

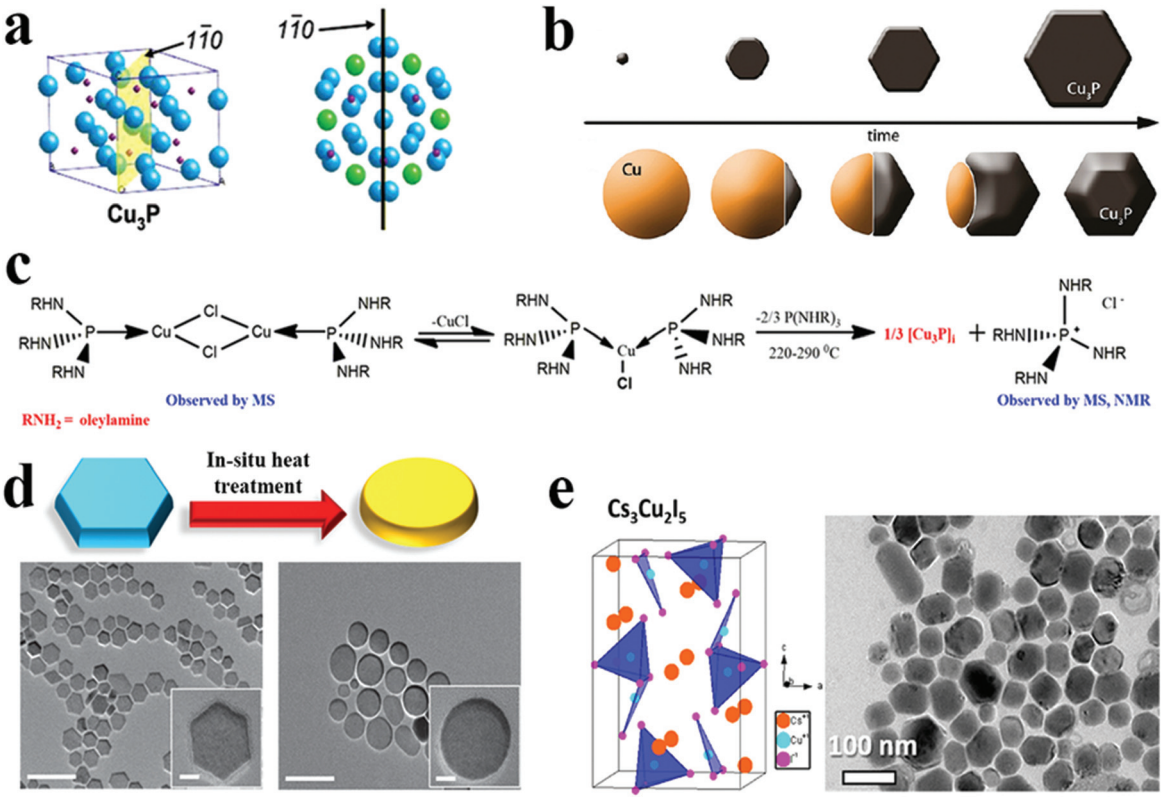


**Fig. 9** (a) $Cu_{3-x}P$ unit cell with the 1$\bar{1}$0 plane highlighted, and top view of numerous unit cells illustrating how the $Cu_{3-x}P$ crystal structure is connected to the nanocrystal hexagonal morphology (Cu atoms with hexagonal patterns emphasised in green, whereas other Cu atoms are blue and phosphorus atoms are red). Reproduced from ref. 69 with permission from ACS, copyright 2007; (b) schematic view of two different synthesis approaches to $Cu_{3-x}P$ NCs. Reproduced from ref. 23 with permission from ACS, copyright 2012; (c) reaction scheme showing the synthesis of $Cu_{3-x}P$ *via* intermediate formation. Reproduced from ref. 136 with permission from ACS, copyright 2021; (d) a schematic representation and TEM images illustrating morphological change that occurred following *in situ* heat treatment of $Cu_{3-x}P$ NCs (scale bars are 100 nm and scale bars in the insets are 10 nm). Reproduced from ref. 50 with permission from Wiley, copyright 2016; (e) crystal structure and transmission electron micrographs of $Cs_3Cu_2I_5$ NPs. Reproduced from ref. 62 with permission from ACS, copyright 2019.


This journal is © The Royal Society of Chemistry 2022

Open Access Article. Published on 27 January 2022. Downloaded on 11/30/2025 6:59:56 AM. This article is licensed under a Creative Commons Attribution 3.0 Unported Licence.

ripening. At the same time, lower TOP/Cu ratios resulted in crystalline Cu NCs.

Manna *et al.* reported a semiconducting and plasmonic 2D platelet-shaped $Cu^{I}$ phosphide using a relatively low-temperature synthesis procedure.[134] In this study, *ex situ* generated phosphine gas was explored as the P source, TOPO as a solvent, and TOP as the nucleation controlling agent. Using more reactive $PH_3$ instead of traditional P sources, such as TOP or TOPO lowered the reaction temperature to 200–230 °C. The tuning of the concentration of TOP resulted in nanoplates of varying sizes from nano to micro. The number of nucleation events varies with the amount of TOP used; a higher amount of TOP reduces the number of nucleation events, resulting in platelets of varying sizes. Furthermore, Liu *et al.* replaced $PH_3$ with $(TMS)_3P$, which increases the reactivity of phosphorus and, consequently, lowers the reaction temperature to as low as 60 °C.[50] They discovered that varying the concentration of TOP affected the average size of hexagonal platelets (Fig. 9d). Subsequently, the colloidal synthesis of $Cu_{3-x}P$ NCs has been reported with the direct nucleation of $Cu_{3-x}P$ using inexpensive, low-toxic, and air-stable triphenyl phosphite as a source of phosphorus by Liu *et al.*[135] This simplified synthesis procedure formed disc-shaped $Cu_{3-x}P$ with a size around 17 nm. Recently, Rachkov *et al.* reported a colloidal synthesis of $Cu_{3-x}P$ nanoplatelets from copper halide salts and tris(diethylamino)phosphine $[P(NEt_2)_3]$ in a one-pot approach.[136] The mass spectrometry and nuclear magnetic resonance spectroscopy study revealed that aminophosphine is first transaminated with a long-chain primary amine. Then the aminophosphine-coordinated metal is disproportionated to give $Cu_{3-x}P$ NCs along with some byproducts (Fig. 9c). Larger nanocrystal sizes were obtained by raising the $P(NEt_2)_3$/Cu, and OLA/phosphorus molar ratios, respectively, but the size of NCs decreased as the reaction temperature decreased. Thus, considerable progress on understanding *ex situ* mechanistic details of growth has been made for $Cu_{3-x}P$ formation. Additionally, the exclusion of TOP as a P source facilitated synthesis at comparatively lower temperatures (<250 °C).

**4.2.2. Ternary Cu-based halides.** The ternary alkali (Rb, Cs) metal copper halides deserve a special mention in the emerging class of colloidally prepared Cu-based NCs. These NCs have gained prominence for LED applications because of their availability, low cost, and environmentally benign nature. The ternary Cu based alkali metal halides possess diverse crystal structures based on the presence of alkali and halide entities at different crystal lattice sites.[151] For example, $CsCu_2I_3$, which is present in the orthorhombic structure (*CmCm*) possesses edge-sharing $CuI_4$ tetrahedra forming one dimensional networks connected through $Cs^+$ units. Contrary to this, in $CsCu_2I_5$ the $CuI_4$ tetrahedral unit shares an edge with the $CuI_3$ triangular unit forming a pseudo pentahedral unit surrounded and isolated by $Cs^+$. Lian *et al.* explained the photoexcitation of such a structure promoted distortion in the structure leading to $Cu^+$ migration and resulting in spindle like $[Cu_2I_5]^{3+}$ units. As a result, the holes accumulate in the $[Cu_2I_5]^{3+}$ like units, and electrons distribute over other sites in the lattice leading to efficient charge separation. This spatial separation of electron and hole results in the self-trapped excitons in alkali metal–copper halide NCs.

Cheng and colleagues reported the first investigation on the colloidal synthesis of caesium copper halide NCs using a hot-injection method.[34] By treating a Cs oleate precursor with Cu(I) halide in ODE, colloidal NCs were synthesised. During the synthesis, $CsCu_2I_3$ nanorods and $Cs_3Cu_2I_5$ nanodiscs were synthesised at two distinct reaction temperatures. Furthermore, they utilised a similar approach to synthesise $Cs_3Cu_2Br_5$ nanoplatelets by using CuBr as a precursor, expanding the library of copper-based two-dimensional anisotropic nanomaterials. Also, Vashishtha *et al.* reported the synthesis of shape- and composition-controlled $Cs_3Cu_2I_5$ nanoplates *via* tailoring the reaction temperature and OLA/oleic acid proportions (Fig. 9e).[62] The injection of Cs-oleate in a solution of copper iodide with a ligand at a lower temperature around 110 °C formed $Cs_3Cu_2I_5$ nanoplates. In contrast, injection at 160 °C resulted in $CsCu_2I_3$ with a nanorod morphology. Here, the reaction temperature was crucial for precise shape tuning, whereas growth time was found to be ineffective for shape tuning, given the high growth rate of these metal halides. Recently, Le *et al.* reported the hot injection synthesis of $Cs_3Cu_2Br_5$ NCs with different chain-length ligands.[137] Acid- and amine-based hydrocarbon ligands were used to improve the solubility of the precursor CuBr. The combination of ligands with different carbon chain lengths (C6, C9 and C18) led to different morphologies. A short ligand (C6) resulted in unevenly shaped, polydisperse NCs due to less control over nucleation and growth with inadequate surface passivation. In comparison, rectangular nanoplates and nanodiscs were developed by combining acid and amine-based ligands with lengths C6/C9 and C9/C18, respectively. The first colloidal $Rb_2CuX_3$ (X = Cl, Br) NCs were synthesised utilising a room-temperature ligand assisted re-precipitation technique by Vashishtha *et al.* The addition of toluene and oleic acid ligands to Rb and Cu halide salts dissolved in DMSO resulted in the formation of NCs.[33] Both structures exhibited a nanoplate-like morphology, with average sizes of 7.7 nm and 7.5 nm for $Rb_2CuBr_3$ and $Rb_2CuCl_3$, respectively. Despite having advantages such as being less toxic and stable, these copper-based halides have poor light-emitting characteristics in comparison with halide perovskites. In addition, a thorough understanding of the influence of morphology on the light-emitting characteristics of Cu based halides is currently missing.

**4.2.3. Metallic Cu-based NCs.** The synthesis of metallic nanocrystals is extensively explored, not only for the improvement of synthetic technology but also for evaluating their electrical, catalytic, sensing, and surface capabilities. Platinum, gold, palladium, copper, and silver nanoparticles, in particular, have risen to the top of the list, owing to a wide range of commercial uses, including catalysis, optoelectronics, sensing, and biological applications and in antibacterial and antiviral drugs.[152–155] Among various metallic NCs, Cu is one of the most promising metallic materials since it is inexpensive, abundant, and highly conductive. The colloidal synthetic tech-

Open Access Article. Published on 27 January 2022. Downloaded on 11/30/2025 6:59:56 AM.
This article is licensed under a Creative Commons Attribution 3.0 Unported Licence.

niques and growth mechanisms for developing diverse morphologies of Cu nanostructures and their usage in numerous technological applications have been extensively researched. In this section, we examine notable examples where 2D anisotropic Cu and Cu–metal alloy NCs are synthesized through colloidal chemistry.

For the synthesis of Cu NCs in the 2D morphology, cetyltrimethylammonium bromide (CTAB), an amphiphilic ligand, is commonly employed. It acts both as a stabilizing and shape-directing agent. For instance, Wang *et al.* achieved the fabrication of single-crystalline Cu nanoplates *via* reducing $Cu^{+}$ using ascorbic acid in the presence of CTAB.[138] Cu NCs with a triangular plate morphology were obtained by varying the pH of the reaction mixture and the concentration of CTAB. The pH of the environment closely governs the ascorbic acid reduction potential and morphology of the NC. At the same time, CTAB forms micelles in the reaction mixture, which serves as a soft template for forming the triangular plate structure (Fig. 10a). Similar observations were reported using ascorbic acid and CTAB by Luc and co-workers where they fabricated freestanding high-quality Cu nanosheets.[139] The Cu nanosheets were found to be triangular in shape with an average edge length of 1.7 ± 0.5 μm. Furthermore, atomic force microscopy revealed the thickness of the Cu nanosheet to be 5 nm. The Cu nanosheets were shown to be stable under ambient conditions, attributed to surface bound ascorbic acid, which inhibited oxidation. In another example, copper(II) acetate was reduced with hydrazine in the presence of *N*,*N*-dimethylformamide (DMF) and polyvinylpyrrolidone (PVP) to produce Cu nanoplates with a diameter of approximately 50 nm and an average thickness of around 20 nm (Fig. 10b).[140] While DMF has been shown to be vital for shape regulation, its specific function remained anonymous.

Copper has been found to be an ideal candidate for alloying with other metals such as Pt, Pd, and Ni. Bimetallic and multimetallic alloy NCs outperform monometallic NCs due to the synergistic impact between/among various metals. For example, ternary FePtCu alloy nanorods surpass binary FePt counterparts and commercial Pt catalysts in catalytic activity and durability in the oxygen reduction reaction (ORR).[156] Cu alloyed with noble metals such as Au provides good stability, optical tunability, and strong catalytic activity and has been utilised in many catalytic processes, including $CO_2$ reduction, *p*-nitrophenol reduction, and catalytic oxidation of benzyl alcohol, CO, and propene.[157–159] Cu has been associated with numerous high cost and low abundant metals such as Pd, Pt, and Au as cost-effective and highly efficient catalysts. Only a few colloidal copper-based metal–metal alloys have been reported to date that exhibit a two-dimensional morphology. For example, Guo *et al.* reported the facile one-pot synthesis of hexagonal and triangular Ni–Cu alloy nanoplates.[24] Distinct Ni(II) reduction and oxidative etching rates at different reaction temperatures influenced the nanoplatelet shapes from hexagonal to triangular. In the same study TOP, a capping agent,

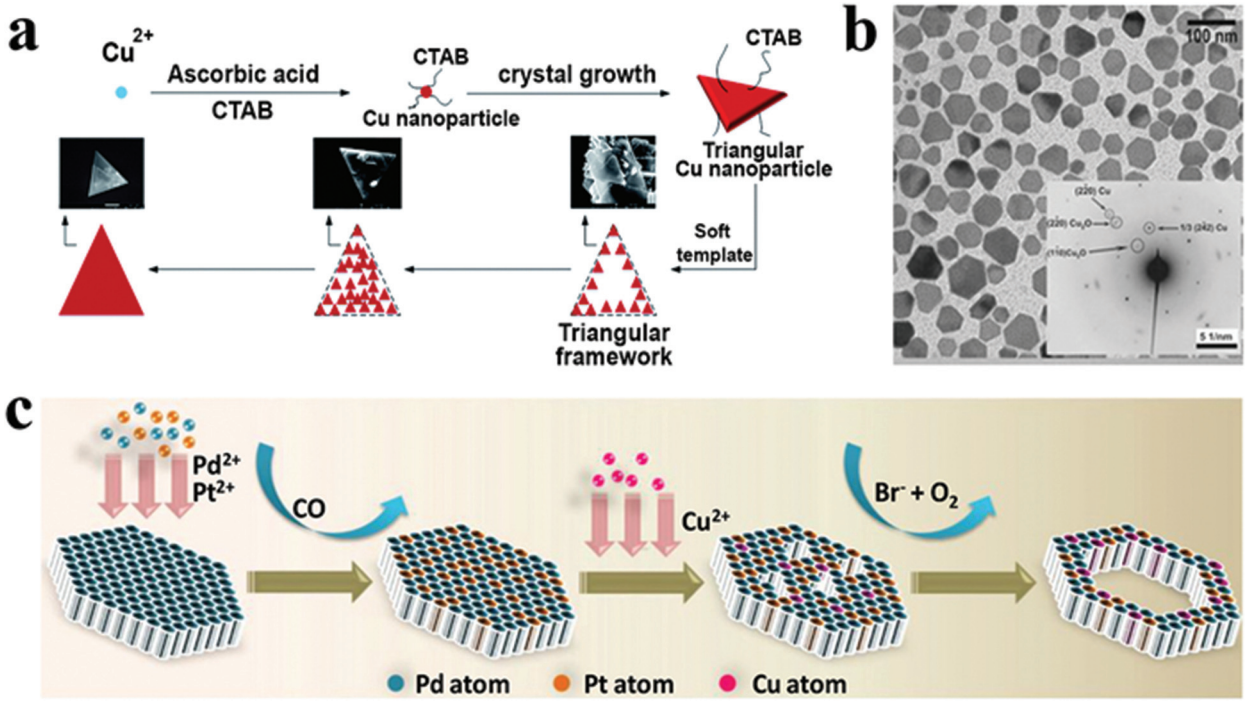


**Fig. 10** (a) Schematic illustrating growth mechanism of Cu nanoplates. Reproduced from ref. 138 with permission from RSC, copyright 2017; (b) TEM image of Cu nanoplates synthesized by the reduction of the Cu precursor by hydrazine in DMF using PVP as the stabilizer. Reproduced from ref. 140 with permission from Wiley, copyright 2009; (c) schematic model illustrating the formation of PdPtCu nanorings. Reproduced from ref. 63 with permission from Wiley, copyright 2021.


This journal is © The Royal Society of Chemistry 2022

Open Access Article. Published on 27 January 2022. Downloaded on 11/30/2025 6:59:56 AM.
This article is licensed under a Creative Commons Attribution 3.0 Unported Licence.

also impacted the kinetics of the reaction and has been shown to control anisotropic shapes. TOP lowered the reaction kinetics, which aided in the formation of the nanoplates, however when TOP was not utilized, the nanosphere shape was formed owing to the rapid reaction kinetics.

Cu has also been alloyed with Pd for heterogeneous catalyst application. For the direct formation of 2D structures,[160] various studies have documented the use of carbonyl salts such as $W(CO)_6$ and $Mo(CO)_6$ as reductants to generate CO molecules that passivate the (111) planes of Pd-based nanosheets. For example, Li *et al.* reported PdPtCu ultrathin nanorings using $W(CO)_6$ as a reductant.[63] Initially, Pd-rich ultrathin nanosheets were synthesized, and these nanosheets were alloyed with Pt to form PdPt nanosheets. Furthermore, PdPt nanosheets were employed as seeds for PdPtCu nanoring formation. When Cu salt is introduced to the reaction system, it starts etching the nanosheet's surface (Fig. 10c). The nanosheets were etched more severely as the reaction continued. After 4 hours, the PdPtCu nanoring morphology was observed. In another study, Yang *et al.* demonstrated the high-yield fabrication of ultrathin 2D PdCu alloy nanosheets with various Cu/Pd atomic ratios.[85] $Mo(CO)_6$ was used initially to reduce Pd(II), which in turn accelerated the reduction of Cu(II), resulting in small PdCu clusters. Furthermore, the PdCu nanosheets were eventually formed due to a seed growth process, and more Cu atoms were embedded into the nanosheets as the process progressed. Very recently, Zhang and coworkers synthesized a PdCu nanoflower shape comprised of multiple 2D nanosheets.[161]

Ag has also been alloyed with Cu among other noble metals to form 2D NCs. For instance, Balkan *et al.* have investigated a one-pot wet-chemical technique for the composition-controlled fabrication of monodisperse CuAg alloy NPs.[141] The fcc type Cu–Ag alloy nanoparticles were formed by co-reducing Cu and Ag metal precursors at 180 °C. The presence of OLA in the reaction facilitated the metal precursor reduction, while oleic acid assisted in narrowing down the size distribution giving monodisperse nanoparticles. Seminal progress has been made towards achieving 2D Cu based metal alloys. However, there are a plethora of compositions such as CuNiPd, PdCuCo, $CuNiPt_6$, CuFeNi, FePtCu, *etc.*, that need to be exploited as 2D NCs to enhance the catalytic efficiency and reduce the cost of production.

# 5. Properties and applications

Owing to the unique characteristics related to their structural features, copper-based 2D NCs have received a lot of interest in plasmonics, heterogeneous catalysis, thermoelectrics and metal-ion batteries.[28,63,141,150,162,163] 2D nanostructures outperform 0D and 1D nanomaterials in architectural modification, charge separation, light harvesting and tunability.[7,164] Extensive research has been done to develop effective catalysts with 2D nanomaterials, inspired by the unique optical, electronic properties and high surface area.[63,162,165] 2D nanostructures with a high surface-area-to-volume ratio and a high density of exposed atoms on their surface hold great promise for enhancing plasmonic resonance and catalytic processes. With the variable valence states, high defect densities, and vast compositional ranges, these NCs have become an ideal choice for the domain of catalysis. With excellent optoelectronic characteristics, Cu based NCs have been exploited as photocatalysts to harvest solar energy.[28,52] They have also been employed as electrocatalysts in oxygen reduction and evolution reactions. In addition, they were found to be suitable for catalysts in synthetic organic chemistry. They are regarded as efficient thermoelectric materials due to the high ionic mobility of $Cu^+$ in the chalcogenide templates that stems for phonon–liquid electron crystal behaviour resulting in suppressed thermal conductivity.[166,167] The 2D shape of these materials stems from complex electronic transport behaviour.[168–170] The in-plane direction possesses a smaller effective mass for electronic transport than the out of plane direction, resulting in greater carrier transport. In the following sub-sections, we cover the range of technological applications of colloidal 2D Cu based NCs.

## 5.1. Plasmonics

The collective oscillation of free-charged carriers related to surface plasmon resonance is the source of plasmonic properties in semiconductor and noble metal bulk materials.[175] In the case of NCs, surface plasmon resonance is localised (localised surface plasmon resonance, LSPR) and can resonate in-phase with the electromagnetic field of light to produce an intense electromagnetic field.[176,177] The enhanced electromagnetic field can convert into heat that functions as heat mediators in photothermal therapy or radiate light that finds application as a concentrator in solar cells, imaging probes, or sensors. Cu based chalcogenides and phosphides represent an exciting class of plasmonic materials where the collective oscillation of holes is the origin of such behaviour.[40,178] 2D anisotropy in these NCs results in two separate LSPR modes *i.e.*, low energy in plane (longitudinal) and high energy out of plane (transverse). The in-plane LSPR peak shifts to a higher wavelength with increased aspect ratio, which can be separated from the out-plane mode, which shifts to a lower wavelength at high aspect ratios.[179] Xie *et al.* observed that the out-plane and in-plane LSPR peaks remain unresolved at a lower aspect ratio of 2 in CuS nanodiscs.[117] However, increasing the aspect ratio two-fold resolved the low intensity out-of plane LSPR peak from the red-shifted in-plane LSPR peak. Recently, Sun *et al.* devised a heat-up approach for synthesising CuS nanodiscs with variable aspect ratio up to ~27. Similarly, they observed red shift in longitudinal LSPR peak from NIR to deep mid-IR with increasing aspect ratio of CuS nanodiscs (Fig. 11a).[171] For the nanodiscs with an aspect ratio of ~27 a low intensity transverse LSPR peak was observed around 900 nm. For low symmetry, 2D morphologies such as triangular and hexa-triangular the transverse peak is more prominent. For instance, Castro *et al.* observed two LSPR peaks at 943 and a longitudinal mode

Open Access Article. Published on 27 January 2022. Downloaded on 11/30/2025 6:59:56 AM.
This article is licensed under a Creative Commons Attribution 3.0 Unported Licence.

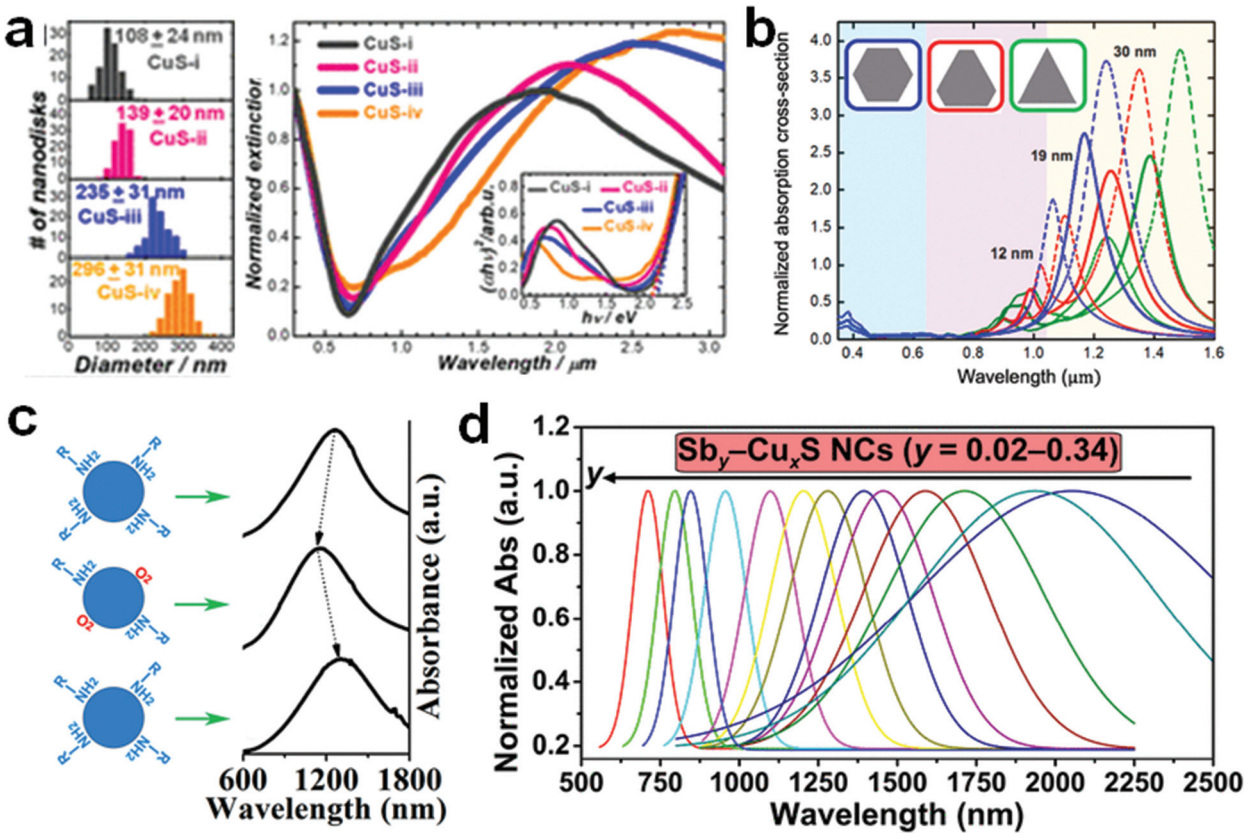


**Fig. 11** (a) Optical extinction spectra displaying a red-shift in the longitudinal LSPR peak with increment in the aspect ratio (fixed thickness of ~11 nm). Reproduced from ref. 171 with permission from ACS, copyright 2021; (b) normalized absorption spectra for CuS nanocrystals of hexagonal, triangular, and hexa-triangular shapes for different lateral dimensions: (dashed line) 12 nm, (solid line) 19 nm, and (dash-dotted line) 30 nm displaying red and blue shift in longitudinal and transverse LSPR peak, respectively. Reproduced from ref. 172 with permission from ACS, copyright 2019; (c) tuning of the LSPR peak by the hole density in CuS air exposure and OLA passivation changing. Reproduced from ref. 173 with permission from ACS, copyright 2013; (d) LSPR tuning of $Cu_xS$ *via* $Sb^{3+}$ doping. Reproduced from ref. 174 with permission from ACS, copyright 2021.

at 1346 nm for triangular CuS nanodiscs. With increasing aspect ratio, a redshift in the longitudinal peak and a blue shift in the transverse LSPR peak were observed (Fig. 11b).[172] However, for more symmetric structures and low dimensions, axial LSPR modes are poorly separated, resulting in broad full width at half maximum.

Tunability of free charge carrier (~$10^{16}$ to $10^{21}$ $cm^{-3}$) concentration by doping can alter the absorption window from visible to near-infrared to (NIR) mid-infrared (MIR) for Cu based chalcogenides which is not possible for noble metals.[180] For example, for Cu-deficient $Cu_{2-x}S$, which possess a diverse phase diagram, the LSPR frequencies can be tuned based on the free hole concentration depending on the Cu/S ratio.[181] Xie *et al.* showcased how LSPR frequency changed depending on hole concentration by adding $Cu^+$ into CuS nanoplatelet templates.[171] Each subsequent addition of $Cu^+$ into the CuS template until Cu/S is 2/1 reduced the hole concentration resulting in fading of LSPR intensity and a red shift in the peak position. In contrast, for $Cu_2S$ and $Cu_2Se$ oxidation induced Cu vacancy increases the hole concentration to modulate LSPR frequency. Wei *et al.* demonstrated the effect of electron donating (Lewis base) and electron accepting (Lewis acid) ligands on modulating the hole density in CuS nanodiscs.[173] Lewis acids such as molecular $O_2$ (from air exposure) and oleic acid, which can act as electron acceptors, increase the hole density by attaching to the NC surface and result in a blue shift of the LSPR peak (Fig. 11c). At the same time, passivation with OLA restores the peak position. Apart from oxidation and reduction-related hole carrier density modulation in self-doped $Cu_xS$, foreign metal cation doping has also been used to tune LSPR.[182,183] Liu *et al.* doped $Sb^{3+}$ in $Cu_xS$ nanodiscs to modulate the LSPR frequency from NIR to mid visible range (Fig. 11d).[174] $Sb^{3+}$ doping induced high carrier density originating from copper vacancy and aliovalent $Sb^{3+}$ and resulted in the LSPR peak shift to a higher energy and narrowing of the full width at half maximum. Thus, stoichiometry is a vital parameter to modulate the hole density for tuning the LSPR frequency. Doping of foreign cations can alter the hole density as well. However, a more controlled way of tuning LSPR frequency is achieving greater control in synthesis, which will ensure desirable stoichiometries with the required morphologies especially with higher asymmetry and aspect ratio for more intense low energy and high energy LSPR modes.


This journal is © The Royal Society of Chemistry 2022

Open Access Article. Published on 27 January 2022. Downloaded on 11/30/2025 6:59:56 AM.
This article is licensed under a Creative Commons Attribution 3.0 Unported Licence.

### 5.2. Thermoelectrics

Thermoelectric (TE) materials are promising as a renewable source for converting waste heat to electricity and *vice versa*.[186,187] However, the conversion efficiency denoted by the TE figure of merit ($ZT$) is yet to reach the benchmark efficiency value of >4 for broader commercial applications.[188] The $ZT$ ($= \sigma S^2 T/k$) depends on the electrical conductivity ($\sigma$), Seebeck coefficient ($S$), and total thermal conductivity ($k$), where the total thermal conductivity is defined by the lattice thermal conductivity ($k_L$) and electrical thermal conductivity ($k_e$). A high-power factor ($\sigma S^2$) and low thermal conductivity are required to achieve a high $ZT$ value. However, controlling these transport properties remains challenging due to their inter-dependent nature. In recent times, the Cu-based chalcogenides having reached $ZT$ values >2 attracted immense attention as viable TE materials.[163,167,185] The copper based binary chalcogenides, especially $Cu_{2-x}S$ and $Cu_{2-x}Se$ display reversible phase transition to highly symmetric phases upon heating to a certain temperature.[166,189] For example, α-$Cu_2Se$ possesses a low symmetry monoclinic crystal structure at room temperature transitions to the cubic β-$Cu_2Se$ phase above 400 K (Fig. 12a).[166] At temperatures above 373 K, $Cu^+$ become highly disordered on the symmetric chalcogen framework resulting a liquid like behaviour responsible for their intrinsic low thermal conductivity. Additionally, nanostructuring of these materials can further reduce the thermal conductivity to a theoretical low value by scattering low and mid frequency phonons (Fig. 12b). Yang *et al.* achieved a $ZT$ value of 1.82 for β-$Cu_2Se$ nanoplates by reducing the $k_L$ 0.11 W $m^{-1}$ $K^{-1}$ *via* forming a high density of small angle grain boundaries and dislocation beneficial for phonon scattering.[190] Similarly, Gahtori utilized nanostructuring of $Cu_2Se$ to reduce the thermal conductivity to 0.34 W $m^{-1}$ $K^{-1}$ which is 65% lower than the bulk thermal conductivity (Fig. 12c) and achieved a $ZT$ value of 2.1 at 973 K.[185] Doping of foreign cations has also been explored as a mean of reducing thermal conductivity or modulating carrier concentration. Liao *et al.* reduced the carrier concentration of α-$Cu_2Se$ from $4.1 \times 10^{20}$ to $2.0 \times 10^{20}$ $cm^{-3}$ at room temperature by doping Bi as the electron donor that reduced $k_e$ and optimized the $ZT$ value to 0.43 at near room temperature of 373 K.[191] Similar to the $Cu_{2-x}Se$, the liquid-like motion of $Cu^+$ in $Cu_{2-x}S$ results in low $\kappa_L$ and high $ZT$ values.[192,193] However, $Cu_{2-x}S$ faces a major problem of S volatilization upon annealing leading to S loss and formation of phases with low Cu deficiency resulting in a low carrier concentration.[194,195] Zhang *et al.* showcased that 0.3% doping of Pb could stabilize the Cu deficient $Cu_{1.8}S$ phase up to 880 K

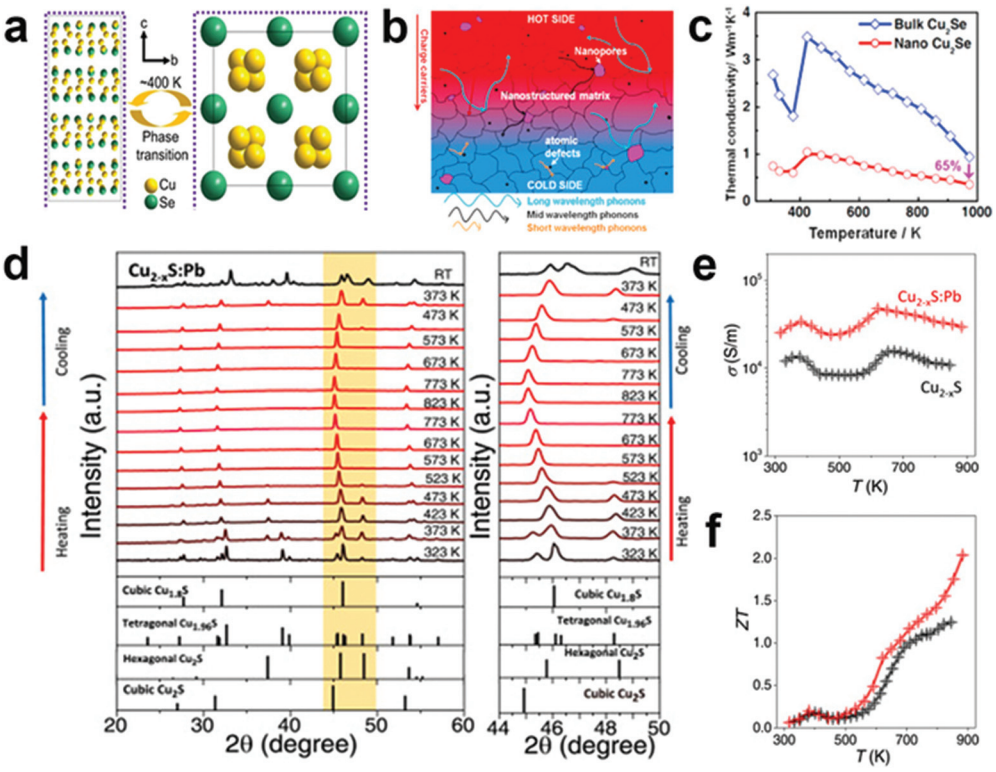


**Fig. 12** (a) Schematic of reversible structural switching between monoclinic α-$Cu_2Se$ and cubic β-$Cu_2Se$; reproduced from ref. 184 with permission from Elsevier, copyright 2020; (b) schematic illustration of phonon scattering associated with nanostructure engineering, (c) 65% reduction in thermal conductivity of $Cu_2Se$ through nanostructuring; reproduced from ref. 185 with permission from Elsevier, copyright 2015; (d) doping of Pb in $Cu_{2-x}S$ stabilized the $Cu_{1.8}S$ phase during annealing resulting in (e) higher electrical conductivity and (f) higher thermoelectric figure of merit. Reproduced from ref. 163 with permission from Elsevier, copyright 2021.

Open Access Article. Published on 27 January 2022. Downloaded on 11/30/2025 6:59:56 AM.
This article is licensed under a Creative Commons Attribution 3.0 Unported Licence.

during Pb:$Cu_{2-x}S$ phase transition enabling a high carrier concentration compared to $Cu_{2-x}S$ (Fig. 12d).[163] Thus, stabilization of the $Cu_{1.8}S$ phase during annealing resulted in a high power factor and a high *ZT* of 2.03 at 880 K (Fig. 12e and f). More complex structures of copper chalcogenides such as tetrahedrite $Cu_{12}Sb_4S_{13}$ have also been explored extensively where a *ZT* of more than 1 was attained.[194] Doping of divalent transition elements by forming $Cu_{12-x}MSb_4S_{13}$ is also a popular way to control their *ZT* by suppressing the number of holes that eventually reduces the $k_e$ resulting in low thermal conductivity. However, most 2D Cu based materials remain unexplored for thermoelectrics. For instance, high entropy multinary NCs and layered NCs which display low thermal conductivities are yet to be utilised.

### 5.3. Photocatalysis

The two major applications of photocatalysis are hydrogen fuel production *via* a water-splitting process utilising sunlight and pollutant dye degradation for wastewater treatment. 2D semiconductor nanomaterials with confined thickness, defined surface area, distinct structural, physical, and chemical characteristics are beneficial in the development of novel photocatalysts. Due to the outstanding visible light absorption properties, non-toxic composition, and environmentally benign nature of different Cu based 2D NCs, they are explored as photocatalysts for harnessing solar energy. Liu *et al.* reported multinary copper chalcogenides $CuGaS_2$ (CGS) NCs with tunable one dimensional and two-dimensional morphologies for photocatalytic hydrogen production.[52] Their research demonstrated that the photocatalytic hydrogen evolution rate (HER) was significantly enhanced by controlling the dimensions. The morphological modification substantially influenced the optical bandgap and energy level of the CGS NCs having 1D and 2D morphologies. These findings are associated with the fraction of exposed {001} and {100} facets. {001} facets were exposed in 2D CGS nanoplates, whereas {100} facets were primarily exposed in 1D wurtzite CGS nanorods (Fig. 13a). In another study, Zhang *et al.* reported copper phosphosulphides as a highly active and stable photocatalyst for hydrogen evolution reactions.[28] Compared to pristine $Cu_{3-x}P$, copper phosphosulphides have a maximal HER of 2085 mol $g^{-1}$ $h^{-1}$, accounting for a five-fold increase in activity. According to the DFT calculations, the phosphosulphide structures push the Gibbs free energies for the intermediate states to be near 0 eV and increase the number of active sites for hydrogen adsorption, resulting in significantly enhanced catalytic activity toward the HER.

Post synthetic modification of copper-based NCs with noble metals has shown enhancement in the catalytic activity. One such example is $Cu_2ZnSnS_4$ (CZTS) nanoplates used as templates to synthesise CZTS–Au and CZTS–Pt heterostructure nanoparticles for hydrogen generation by water splitting and degradation of water pollutants (Fig. 13b).[196] Through effective

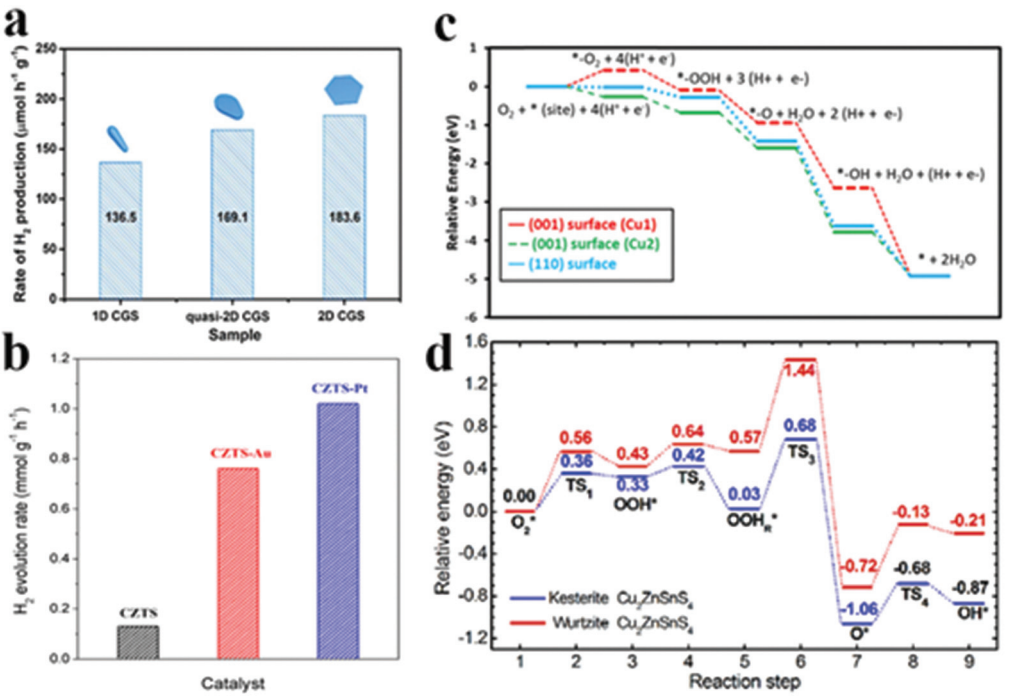


**Fig. 13** (a) The photocatalytic hydrogen generation rates for 1D CGS nanorods, quasi-2D nanodiscs, and 2D CGS nanoplates. Reproduced from ref. 52 with permission from RSC, copyright 2019; (b) the rate of hydrogen evolution in post-modified CZTS–Au and CZTS–Pt heterostructure nanoparticles, along with pristine CZTS. Reproduced from ref. 196 with permission from ACS, copyright 2016; (c) energy profile diagram of the ORR for Cu (1)-terminated (001) surfaces (red), Cu (2)-terminated (001) surfaces (blue), and (110) surfaces (green). Reproduced from ref. 197 with permission from ACS, copyright 2018. (d) Reaction free-energy diagrams for the ORR on kesterite (blue) and wurtzite CZTS (red). Reproduced from ref. 196 with permission from ACS, copyright 2016.

 This journal is © The Royal Society of Chemistry 2022

Open Access Article. Published on 27 January 2022. Downloaded on 11/30/2025 6:59:56 AM.
This article is licensed under a Creative Commons Attribution 3.0 Unported Licence.

charge transfer of photogenerated carriers from the semiconductor to metal co-catalysts promoted solar energy conversion. The co-catalyst decreased the overpotential of the reaction, lowering the charge carrier transfer interface barrier and enhancing surface redox processes such as water splitting and dye degradation. Cui *et al.* demonstrated $Cu_7S_4$@Pd hetero nanostructures for high-efficiency photocatalytic reactions such as the Suzuki coupling reaction, nitrobenzene hydrogenation, and benzyl alcohol oxidation. $Cu_7S_4$@Pd enabled hot-carrier transfer from $Cu_7S_4$ to Pd, which accelerated catalytic processes on the Pd metallic surface.[29] For all three types of organic reactions, hetero nanostructures exhibited remarkable catalytic activity, with over 80–100% conversion accomplished in less than 2 hours.

Cu chalcogenides' plasmonic characteristics have also been explored to enhance the photocatalytic degradation of contaminants and dyes. Shao *et al.*, for example, illustrated the use of such plasmonic $Cu_{2-x}S$ nanoparticles for rhodamine B and methyl orange degradation.[198] Their study shows that photocatalytic activity could be regulated and controlled by modulating carrier concentrations. For example, $Cu_{1.94}S$ NCs with the highest free carrier density exhibited the best photocatalytic activity compared to $Cu_{1.2}S$ NC. $Cu_{1.94}S$ NCs degraded over 80% of the dye molecules in the first 20 minutes, compared to $Cu_{1.2}S$ NCs, which degraded only 57% of the dye molecules after 120 minutes of UV exposure. In another instance, $Cu_{2-x}S_ySe_{1-y}$ NCs have been demonstrated to be a potent photo-activated catalyst for the Huisgen [3 + 2] cycloaddition process.[199] Here, the NCs serve as an efficient photocatalyst by generating Cu(I) into the solution when irradiated, providing fascinating new avenues for doing such archetypal click chemistry.

Post-modification of copper phosphide has become an avenue for the plethora of efficient photo and photo electrocatalysts. Dutta *et al.* described an oriented attachment of Au and $Cu_{3-x}P$ to develop a novel ring-on-disc heterostructure.[200] The addition of phosphine gas as a bridging agent to the reaction mixture guided the pre synthesised Au nanoparticles onto the edges of $Cu_{3-x}P$ discs, resulting in a unique heterostructure. Furthermore, the Au–$Cu_{3-x}P$ has been employed as a photocatalyst for the evolution of hydrogen from water. Since the coupling of exciton and plasmon inhibits excitonic recombination and thus promotes the photo-electron transfer process, making Au–$Cu_{3-x}P$ a better photocatalyst than pristine $Cu_{3-x}P$. In another instance, thin Au nanowires grown in a stripy patterned pattern on $Cu_{3-x}P$ platelets are investigated as photoanode materials for the catalytic oxidation of an essential biomolecule, nicotinamide adenine dinucleotide (NADH).[32] In the presence of NADH, Au–$Cu_{3-x}P$ exhibited a more than 30-fold rise in current density compared to its absence. Thus, the functionalisation of the 2D NC surface with various capping agents and metal NCs has proven to be highly significant for enhancing catalytic activity.

### 5.4. Electrocatalysis

Electrocatalysis has recently received much attention due to its application in fuel cells, electrolysis, and other energy storage and conversion reactions.[25] In general, charge transport at electrode/electrolyte interfaces has a substantial influence on electrocatalytic activity.[162] Pt-free electrocatalysts composed of 2D Cu-based NCs offer potential benefits such as low cost, comparative electrochemical activity to precious metals, and adjustable physical and chemical characteristics. Implementing a 2D ultrathin nanostructure can enhance accessible active sites and improve the electronic conductivity in electrocatalysis. Cu deficient $Cu_{2-x}S$ nanoplates are demonstrated as active oxygen reduction reaction (ORR) electrocatalysts with increased ORR activity when the free hole concentration in $Cu_{2-x}S$ was increased.[68] Additionally, post-modified $Cu_{2-x}S$ nanoplates with carbon black demonstrated a significant increase in activity compared to $Cu_{2-x}S$ alone due to increased electrical conductivity and synergistic effect between $Cu_{2-x}S$ and graphene. The electrochemical performance of anisotropic size-tunable 2D CuS nanoplatelets has been comprehensively studied by Liu *et al.*[197] CuS nanoplatelets with a uniform thickness, but a broadly variable diameter demonstrated electrochemical activity for the oxygen reduction reaction in alkaline solution. The activity of the oxygen reduction process in alkaline solution enhanced as the diameter was increased (Fig. 13c). $Cu_{2-x}S$ NC's electrochemical activity was found to be strongly facet-dependent and anisotropic. Increasing the diameter of NCs promotes charge carrier transport through the electrocatalyst layer while maintaining the specific surface area of the most electrochemically active facets. Yu *et al.* reported two phases of $Cu_2ZnSnS_4$ (CZTS) NCs and examined their catalytic activity targeting the ORR.[196] Higher oxidation states, such as $Zn^{2+}$ and $Sn^{4+}$, give more energetically favourable sites for oxygen adsorption and subsequent hydroxyl production. CZTS NCs demonstrated ORR activity comparable to commercial Pt/C electrocatalysts, with high current densities (5.45 mA $cm^2$ at 0.1 V *vs.* RHE) and low onset reduction potential (0.89 V *vs.* RHE). $Sn^{4+}$ and $Zn^{2+}$ sites offered low energy barriers for the rate-determining phase and enhanced electrocatalytic activity. The catalytic reactivity is influenced mainly by the shape and primarily exposed crystal planes. The two exposed planes in 2D materials (Fig. 13d) can have distinct electrocatalytic reactions. Zhao *et al.* successfully synthesised ultrathin $CuCo_2S_4$ nanosheets (NSs) with predominantly exposed {111}, {022}, and {004} planes.[201] In terms of the oxygen reduction reaction/oxygen evolution reaction (ORR/OER), the two exposed planes (022) and (004) have distinct preferences. Therefore, the $CuCo_2S_4$ NCs display outstanding bifunctional catalytic capabilities toward both the ORR and OER in alkaline solutions and $CuCo_2S_4$ nanosheets outperform commercial Pt/C electrocatalysts well as $CuCo_2S_4$ nanoparticles in electrochemical activity. Park *et al.* synthesised $Pd_{13}Cu_3S_7$ nanoplates *via* partial cation exchange of $Cu_{1.81}S$ with the Pd precursor and investigated their electrocatalytic activity for the HER.[30] This $Pd_{13}Cu_3S_7$ NCs showed an overpotential of only 64.0 mV at −10 mA $cm^{-2}$ and a Tafel slope of 49.6 mV $dec^{-1}$, making them one of the finest sulphide-based catalysts for the HER comparable to the commercial Pd/C catalysts. In another report, Li *et al.* investigated Co-doped $Cu_7S_4$ nanodiscs as

Open Access Article. Published on 27 January 2022. Downloaded on 11/30/2025 6:59:56 AM.
This article is licensed under a Creative Commons Attribution 3.0 Unported Licence.

highly efficient electrocatalysts for oxygen evolution reactions.[202] In comparison to bare $Cu_7S_4$, the developed catalyst exhibited a low overpotential of 270 mV to reach a current density of 10 mA $cm^{-2}$ and with a reduced Tafel slope and improved turnover frequencies. Thus, the heterostructure formation and cationic doping have proven significant for enhancing the catalytic activity of the semiconductor NCs. The copper–metal alloy nanocrystals have the potential to replace commercial Pt/C for various electrocatalytic reactions. Alloying noble elements with Earth-abundant Cu becomes a realistic, simple, and successful method for lowering the cost of electrocatalysts while increasing their catalytic performance. Several 2D copper-based alloys have been utilized as a catalyst for electrocatalytic reactions. For example, the composition-dependent electrocatalytic activities of CuAg alloy nanocrystals in ORR have been reported.[141] CuAg NCs outperform pristine Ag by about 1.5 times in ORR activity. Furthermore, with increased Cu content, electrochemical impedance spectroscopy revealed lower charge transfer resistance. The optimal composition was discovered to be $Cu_{40}Ag_{60}$, and its increased activity was attributed to changes in the electrical structure caused by alloying. In another study, in alkaline circumstances, PdPtCu nanorings have been employed as efficient and long-lasting electrocatalysts for the ORR.[85] This catalyst achieves an ultrahigh electrochemical active surface area, significantly more than the commercial Pt/C catalyst, leading to an enhanced ORR activity. Furthermore, the catalyst demonstrated consistent endurance, with an activity retention of 86% after 30 000 cycles. Post-modified PdCu alloy nanosheets have shown a high activity towards formic acid oxidation.[161] The elevated activity has been attributed to the ultrathin morphology, a synergistic impact between Pd and Cu, and post-treatment.

Despite many theoretical calculations and *ex situ* observations, no firm conclusions on determining the actual active sites for catalytic processes have been reached yet. As a result, a comprehensive *in situ* study is required to elucidate the unique active sites for various catalytic processes. Considering the high potential of Cu based catalysts, there is still a gap in meeting commercial needs, offering an opportunity to increase the catalytic activity further. Understanding facet-specific binding with *in situ* X-ray absorption near-edge spectroscopy (XANES) and extended X-ray absorption fine structure (EXAFS) and simulation of crystal facets with active species will be beneficial to enhance catalytic activity further.

### 5.5. Other applications

The ubiquity of the application of 2D Cu based NCs has also been extended to electrodes for batteries and sensors. One of their notable applications is in lithium-ion batteries (LIBs), where the $Cu_{2-x}E$ based anode undergoes a conversion mechanism forming $Li_2E$ and Cu (Fig. 14a). In this regard, the copper telluride nanostructure with different morphologies ranging from nanocubes, nanosheets, and nanoparticles have been tested as an anode in lithium-ion batteries.[31] Among all the nanosheet, nanocube, or nanoparticle electrodes, the $Cu_{2x}Te$ nanosheet electrode offered the highest capacity and best rate capability (Fig. 14b). The superior electrical contact and homogeneity of nanosheets over nanoparticles or nanocubes contributed to the outstanding performance of the nanosheet anode.

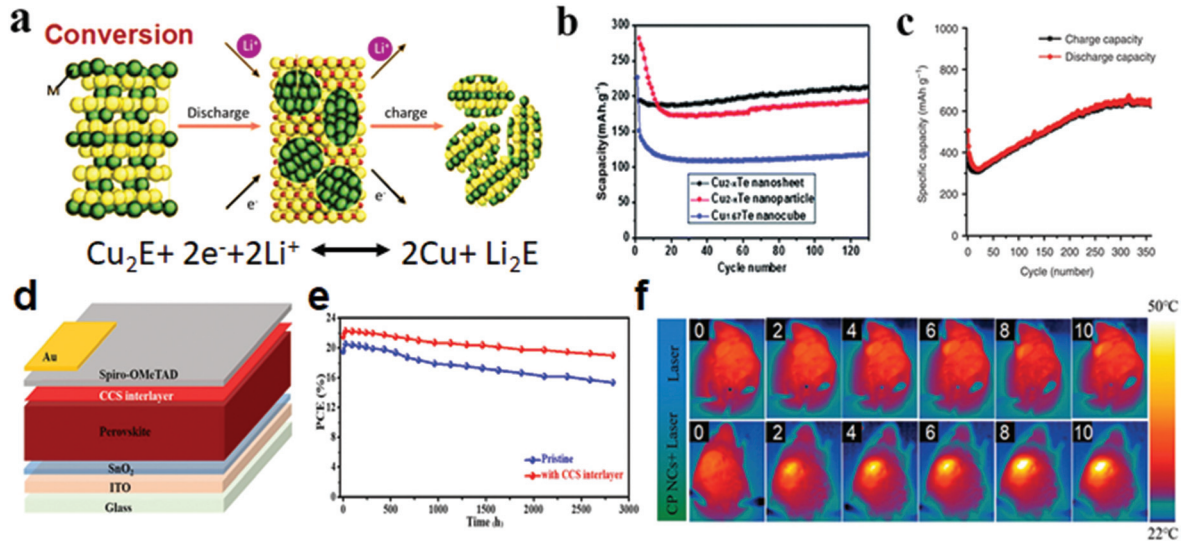


Fig. 14 (a) Schematic of the conversion reaction of copper chalcogenide anodes (E = S, Se, Te) in lithium ion batteries (LIB); (b) specific capacity at a rate of 0.5C for three different $Cu_{2-x}Te$ based anodes in LIB; reproduced from ref. 31 with permission from RSC, copyright 2014; (c) specific capacity at a current density of 0.2 A $g^{-1}$ of CuS nanosheet based anode in LIB; reproduced from ref. 74 with permission from Nature, copyright 2012; (d) a schematic cross-sectional representation of the device architecture consisting of the $CsCu_5S_3$ NC interlayer, (e) stability of unencapsulated PSCs without and with a $CsCu_5S_3$ interlayer. Reproduced from ref. 65 with permission from Elsevier, copyright 2021; (f) *in vivo* thermal images of tumor-bearing mice. Reproduced from ref. 203 with permission from Wiley, copyright 2019.

 This journal is © The Royal Society of Chemistry 2022

Open Access Article. Published on 27 January 2022. Downloaded on 11/30/2025 6:59:56 AM.
This article is licensed under a Creative Commons Attribution 3.0 Unported Licence.

Furthermore, the assembled cell composed of $Cu_{2x}Te$ NCs displayed extremely high cycling stability (up to 5000 cycles). This example clearly demonstrates the significance of regulating the morphology for improved performance. Kim *et al.* studied the electrochemical performance of CuS nanosheets as an electrode for LIBs. They obtained a specific capacity of 642 mA h $g^{-1}$ after 270 cycles at a current density of 0.2 A $g^{-1}$ (Fig. 14c).[74] Being a conversion material, CuS shows a theoretical capacity of 560 mA h $g^{-1}$ for Li ion batteries. However, the expulsion of Cu from CuS upon $Li_2S$ formation disassembled the nanosheets and increased the exposed surface area for more Li reactivity, resulting in higher capacity than usual CuS based electrodes.

Apart from application in batteries, CuSe nanosheets have been employed for flexible electronics by making conductive films.[204] Films coated with CuSe hexagonal nanosheets exhibited ohmic activity, with a conductivity of 535 S $m^{-1}$ that sustained for several months in the air. In another study, Sun and co-workers reported the integration of graphene with colloidal $Cu_{3-x}P$ 2D quantum dots for optoelectronic applications.[178] These hybrids demonstrated high broadband operation capability as well as good flexibility. Recently, hexagonal $CsCu_5S_3$ NCs were employed as an interlayer between the perovskite film and the hole transport layer in perovskite solar cells (Fig. 14d).[65] This interlayer enhanced the hole transport while acting as an energy barrier to minimise carrier recombination, resulting in a power conversion efficiency of 22.29% (Fig. 14e). In another instance, a high-energy Q-switched laser using plasmonic $Cu_{3-x}P$ NCs as effective nonlinear absorbers has been reported.[50] $Cu_{3-x}P$ NCs exhibit comparable nonlinear optical characteristics and device performance to other Q-switchers and improved compatibility with optical components.

In recent years, copper chalcogenide based 2D nanomaterials have shown great potential in the biomedical field. Copper chalcogenide-based 2D nanomaterials have recently emerged as effective photothermal agents for photothermal treatment (PTT) owing to their attractive low cost, low toxicity, biodegradability and high absorption of near-infrared (NIR) light across a relatively wide wavelength range.[122,205] He *et al.* reported plasmonic CuS nanodisc based composite nanocapsules for chemo-photothermal cancer therapy.[206] In another study, CuTe NCs spanning from 1D to 3D morphologies were explored as photothermal agents and surface-enhanced Raman scattering probes. With enhancement factors of $1.5 \times 10^6$ and $10^6$, respectively, CuTe nanocubes and nanoplates produced excellent signal-to-noise spectra, whereas CuTe nanorods did not yield any SERS signal. Recently, Wang and co-workers investigated photoacoustic ovarian tumour imaging with CuS nanodiscs and nanoprisms. CuS nanodiscs and nanoprisms both generated sensitive photoacoustic signals in the picomolar range.[67] Liu and co-workers reported a $Cu_{3-x}P$ NCs based Fenton agent for *in situ* self-generation T1-MRI-guided PTT and PT-enhanced CDT.[203] $Cu_{3-x}P$ NCs potentially generated a high quantity of toxic $^{\bullet}OH$ in response to over-expressed $H_2O_2$ in tumour tissue. Furthermore, the tumour's excess GSH can decrease Cu(II) generated in the Fenton-like reaction to Cu(I), boosting the rate of $^{\bullet}OH$ production. (Fig. 14f). This study shed insights into the approach towards generating more Fenton-like agents that are both revolutionary and efficient.

## 6. Challenges and future directions

In summary, we have highlighted the research progress made on the synthesis and applications of 2D Cu based NCs, Cu-chalcogenides, phosphides, halides, and Cu–metal alloys. Though these NCs are promising due to their cost-effective and environmentally benign nature, they are still lagging behind heavy chalcogenides in terms of optoelectronic properties due to limitations associated with ultrathin NC formation. To date, ultrathin nanosheets of $Cu_{2-x}S$ and In-poor CuInS have been successfully synthesized based on soft templated growth and self-organization, respectively. However, transformation into multinary composition in most other instances is dependent on cation exchange. Hence, future exploration is necessary for the direct growth of ultrathin nanosheets with multinary compositions. Here, the real-time study of nucleation and growth kinetics such as liquid cell *in situ* TEM, small-angle X-ray scattering (SAXS), X-ray absorption near-edge spectroscopy (XANES) and extended X-ray absorption fine structure (EXAFS) spectroscopy for these existing NCs will provide insights into the design of ultrathin NCs of complex multinary composition including $Cu_{3-x}P$, Cu–metal alloys, and Cu-halides.[207] The $Cu^+$ mobility in the $Cu_{3-x}P$ template is similar to the Cu-chalcogenides. However, the formation of multinary NCs based on $Cu_{3-x}P$ has not been explored except for $Cu_3P_{1-x}S_x$. The Cu-halides, which have shown more stability than lead based perovskites, self-trapped emissions, longer lifetime, and wide bandwidths, are promising for lighting devices. Nevertheless, the moisture stability is not good enough for large scale device fabrications. Here the shell formation of metal chalcogenides such as ZnS will enhance the stability.[208]

The layered 2D Cu-based NCs are expected to show low thermal conductivities resulting from low phonon group velocity and lattice anharmonicity from weak interaction between layers and heterogeneity in chemical bonding. However, each monolayer exhibits quantum confinement of charge carriers resulting in a high Seebeck coefficient, ideal for efficient thermoelectric performance. Here, apart from $CuCrSe_2$, other layered structures such as $CuME_2$ (M = Mo, W, E = S, Se) and $ACuME_2$ (A = Na, K, Cs, Rb, M = Mn, Fe, Co, Ni, Zn) remain unexplored as NCs in thermoelectrics. Furthermore, the Kirkendall effect is another less explored yet effective tool for synthesizing hollow morphologies with more active sites for electrochemical reactions. Therefore, the Cu-based 2D NC family, which comprises a massive library of NCs with different phases and compositions, holds great promise as future 2D materials for energy applications.

## Conflicts of interest

There are no conflicts to declare.

Open Access Article. Published on 27 January 2022. Downloaded on 11/30/2025 6:59:56 AM.
This article is licensed under a Creative Commons Attribution 3.0 Unported Licence.

## Acknowledgements

NK acknowledges financial support of the Irish Research Council (IRC) under Grant Number IRCLA/2017/285. NP acknowledges financial support from the Department of Chemical Sciences, University of Limerick. The authors also acknowledge Science Foundation Ireland (SFI) under the Principal Investigator Program under contract no. 16/IA/4629 and under grant no. SFI 16/M-ERA/3419.

## Notes and references

1 P. S. Zhou, P. Schiettecatte, M. Vandichel, A. Rousaki, P. Vandenabeele, Z. Hens and S. Singh, *Cryst. Growth Des.*, 2021, **21**, 1451.
2 Y. F. Sun, M. Terrones and R. E. Schaak, *Acc. Chem. Res.*, 2021, **54**, 1517.
3 P. S. Zhou, G. Collins, Z. Hens, K. M. Ryan, H. Geaney and S. Singh, *Nanoscale*, 2020, **12**, 22307.
4 Y. F. Sun, Y. X. Wang, J. Y. C. Chen, K. Fujisawa, C. F. Holder, J. T. Miller, V. H. Crespi, M. Terrones and R. E. Schaak, *Nat. Chem.*, 2020, **12**, 284.
5 M. S. Sokolikova and C. Mattevi, *Chem. Soc. Rev.*, 2020, **49**, 3952.
6 A. C. Berends and C. D. Donega, *J. Phys. Chem. Lett.*, 2017, **8**, 4077.
7 M. Nasilowski, B. Mahler, E. Lhuillier, S. Ithurria and B. Dubertret, *Chem. Rev.*, 2016, **116**, 10934.
8 J. S. Son, J. H. Yu, S. G. Kwon, J. Lee, J. Joo and T. Hyeon, *Adv. Mater.*, 2011, **23**, 3214.
9 D. D. Vaughn, R. J. Patel, M. A. Hickner and R. E. Schaak, *J. Am. Chem. Soc.*, 2010, **132**, 15170.
10 F. Li, M. M. R. Moayed, E. Klein, R. Lesyuk and C. Klinke, *J. Phys. Chem. Lett.*, 2019, **10**, 993.
11 S. Jeong, D. Yoo, J. T. Jang, M. Kim and J. Cheon, *J. Am. Chem. Soc.*, 2012, **134**, 18233.
12 J. H. Han, S. Lee and J. Cheon, *Chem. Soc. Rev.*, 2013, **42**, 2581.
13 L. W. Dai, C. Strelow, T. Kipp, A. Mews, I. Benkenstein, D. Eifler, T. H. Vuong, J. Rabeah, J. McGettrick, R. Lesyuk and C. Klinke, *Chem. Mater.*, 2021, **33**, 275.
14 L. Sonntag, V. Shamraienko, X. L. Fan, M. S. Khoshkhoo, D. Kneppe, A. Koitzsch, T. Gemming, K. Hiekel, K. Leo, V. Lesnyak and A. Eychmuller, *Nanoscale*, 2019, **11**, 19370.
15 T. Galle, M. S. Khoshkhoo, B. Martin-Garcia, C. Meerbach, V. Sayevich, A. Koitzsch, V. Lesnyak and A. Eychmuller, *Chem. Mater.*, 2019, **31**, 3803.
16 S. Delikanli, G. N. Yu, A. Yeltik, S. Bose, T. Erdem, J. H. Yu, O. Erdem, M. Sharma, V. K. Sharma, U. Quliyeva, S. Shendre, C. Dang, D. H. Zhang, Z. C. Sum, W. J. Fan and H. V. Demir, *Adv. Funct. Mater.*, 2019, **29**, 1901028.
17 L. W. Dai, R. Lesyuk, A. Karpulevich, A. Torche, G. Bester and C. Klinke, *J. Phys. Chem. Lett.*, 2019, **10**, 3828.
18 E. Izquierdo, A. Robin, S. Keuleyan, N. Lequeux, E. Lhuillier and S. Ithurria, *J. Am. Chem. Soc.*, 2016, **138**, 10496.
19 V. Dzhagan, A. G. Milekhin, M. Y. Valakh, S. Pedetti, M. Tessier, B. Dubertret and D. R. T. Zahn, *Nanoscale*, 2016, **8**, 17204.
20 S. Singh, R. Tomar, S. ten Brinck, J. De Roo, P. Geiregat, J. C. Martins, I. Infante and Z. Hens, *J. Am. Chem. Soc.*, 2018, **140**, 13292.
21 A. C. Berends, J. D. Meeldijk, M. A. van Huis and C. D. Donega, *Chem. Mater.*, 2017, **29**, 10551.
22 K. Ramasamy, H. Sims, W. H. Butler and A. Gupta, *J. Am. Chem. Soc.*, 2014, **136**, 1587.
23 L. De Trizio, A. Figuerola, L. Manna, A. Genovese, C. George, R. Brescia, Z. Saghi, R. Simonutti, M. Van Huis and A. Falqui, *ACS Nano*, 2012, **6**, 32.
24 H. Z. Guo, Y. Z. Chen, H. M. Ping, L. S. Wang and D. L. Peng, *J. Mater. Chem.*, 2012, **22**, 8336.
25 Y. T. Guntern, V. Okatenko, J. Pankhurst, S. B. Varandili, P. Iyengar, C. Koolen, D. Stoian, J. Vavra and R. Buonsanti, *ACS Catal.*, 2021, **11**, 1248.
26 P. Reiss, M. Carriere, C. Lincheneau, L. Vaure and S. Tamang, *Chem. Rev.*, 2016, **116**, 10731.
27 K. Ramasamy, R. K. Gupta, H. Sims, S. Palchoudhury, S. Ivanov and A. Gupta, *J. Mater. Chem. A*, 2015, **3**, 13263.
28 X. Zhang, K. A. Min, W. Zheng, J. Hwang, B. Han and L. Y. S. Lee, *Appl. Catal., B*, 2020, **273**, 118927.
29 J. B. Cui, Y. J. Li, L. Liu, L. Chen, J. Xu, J. W. Ma, G. Fang, E. B. Zhu, H. Wu, L. X. Zhao, L. Y. Wang and Y. Huang, *Nano Lett.*, 2015, **15**, 6295.
30 J. Park, H. Jin, J. Lee, A. Oh, B. Kim, J. H. Kim, H. Baik, S. H. Joo and K. Lee, *Chem. Mater.*, 2018, **30**, 6884.
31 C. Han, Z. Li, W. J. Li, S. L. Chou and S. X. Dou, *J. Mater. Chem. A*, 2014, **2**, 11683.
32 A. Dutta, A. K. Samantara, S. Das Adhikari, B. K. Jena and N. Pradhan, *J. Phys. Chem. Lett.*, 2016, **7**, 1077.
33 P. Vashishtha, T. J. N. Hooper, Y. N. Fang, D. Kathleen, D. Giovanni, M. Klein, T. C. Sum, S. G. Mhaisalkar, N. Mathews and T. White, *Nanoscale*, 2021, **13**, 59.
34 P. F. Cheng, L. Sun, L. Feng, S. Q. Yang, Y. Yang, D. Y. Zheng, Y. Zhao, Y. B. Sang, R. L. Zhang, D. H. Wei, W. Q. Deng and K. L. Han, *Angew. Chem., Int. Ed.*, 2019, **58**, 16087.
35 Y. K. Jung, I. T. Han, Y. C. Kim and A. Walsh, *npj Comput. Mater.*, 2021, **7**, 51.
36 N. Kapuria, U. V. Ghorpade, M. Zubair, M. Mishra, S. Singh and K. M. Ryan, *J. Mater. Chem. C*, 2020, **8**, 13868.
37 Y. Liu, M. X. Liu, D. Q. Yin, W. Wei, P. N. Prasad and M. T. Swihart, *Chem. Mater.*, 2017, **29**, 3555.
38 H. R. Ning, Y. Zeng, S. W. Zuo, S. V. Kershaw, Y. Hou, Y. Y. Li, X. N. Li, J. Zhang, Y. P. Yi, L. H. Jing, J. Li and M. Y. Gao, *ACS Nano*, 2021, **15**, 873.
39 E. Lhuillier, S. Pedetti, S. Ithurria, B. Nadal, H. Heuclin and B. Dubertret, *Acc. Chem. Res.*, 2015, **48**, 22.
40 C. Coughlan, M. Ibanez, O. Dobrozhan, A. Singh, A. Cabot and K. M. Ryan, *Chem. Rev.*, 2017, **117**, 5865.
41 X. Q. Chen, J. P. Yang, T. Wu, L. Li, W. Luo, W. Jiang and L. J. Wang, *Nanoscale*, 2018, **10**, 15130.

 This journal is © The Royal Society of Chemistry 2022

Open Access Article. Published on 27 January 2022. Downloaded on 11/30/2025 6:59:56 AM.
This article is licensed under a Creative Commons Attribution 3.0 Unported Licence.

42 M. V. Kovalenko, L. Manna, A. Cabot, Z. Hens, D. V. Talapin, C. R. Kagan, V. I. Klimov, A. L. Rogach, P. Reiss, D. J. Milliron, P. Guyot-Sionnnest, G. Konstantatos, W. J. Parak, T. Hyeon, B. A. Korgel, C. B. Murray and W. Heiss, *ACS Nano*, 2015, **9**, 1012.
43 Y. Chen, Z. X. Fan, Z. C. Zhang, W. X. Niu, C. L. Li, N. L. Yang, B. Chen and H. Zhang, *Chem. Rev.*, 2018, **118**, 6409.
44 Y. A. Yang, H. M. Wu, K. R. Williams and Y. C. Cao, *Angew. Chem., Int. Ed.*, 2005, **44**, 6712.
45 X. G. Peng, J. Wickham and A. P. Alivisatos, *J. Am. Chem. Soc.*, 1998, **120**, 5343.
46 C. B. Murray, D. J. Norris and M. G. Bawendi, *J. Am. Chem. Soc.*, 1993, **115**, 8706.
47 A. C. Berends, W. van der Stam, Q. A. Akkerman, J. D. Meeldijk, J. van der Lit and C. D. Donega, *Chem. Mater.*, 2018, **30**, 3836.
48 W. Bryks, M. Wette, N. Velez, S. W. Hsu and A. R. Tao, *J. Am. Chem. Soc.*, 2014, **136**, 6175.
49 W. van der Stam, F. T. Rabouw, J. J. Geuchies, A. C. Berends, S. O. M. Hinterding, R. G. Geitenbeek, J. van der Lit, S. Prevost, A. V. Petukhov and C. D. Donega, *Chem. Mater.*, 2016, **28**, 6381.
50 Z. K. Liu, H. R. Mu, S. Xiao, R. B. Wang, Z. T. Wang, W. W. Wang, Y. J. Wang, X. X. Zhu, K. Y. Lu, H. Zhang, S. T. Lee, Q. L. Bao and W. L. Ma, *Adv. Mater.*, 2016, **28**, 3535.
51 S. Das Adhikari, A. Dutta, G. Prusty, P. Sahu and N. Pradhan, *Chem. Mater.*, 2017, **29**, 5384.
52 Z. M. Liu, J. Liu, Y. B. Huang, J. Li, Y. Yuan, H. H. Ye, D. X. Zhu, Z. J. Wang and A. W. Tang, *Nanoscale*, 2019, **11**, 158.
53 J. J. Wang, Y. Q. Wang, F. F. Cao, Y. G. Guo and L. J. Wan, *J. Am. Chem. Soc.*, 2010, **132**, 12218.
54 C. Coughlan, Y. N. Guo, S. Singh, S. Nakahara and K. M. Ryan, *Chem. Mater.*, 2018, **30**, 8679.
55 C. Behera, R. Samal, C. S. Rout, R. S. Dhaka, G. Sahoo and S. L. Samal, *Inorg. Chem.*, 2019, **58**, 15291.
56 S. Bera, S. Shyamal, S. Sen and N. Pradhan, *J. Phys. Chem. C*, 2020, **124**, 15607.
57 S. Lee, S. Baek, J. P. Park, J. H. Park, D. Y. Hwang, S. K. Kwak and S. W. Kim, *Chem. Mater.*, 2016, **28**, 3337.
58 J. F. L. Lox, Z. Y. Dang, M. L. Anh, E. Hollinger and V. Lesnyak, *Chem. Mater.*, 2019, **31**, 2873.
59 J. J. Wang, P. Liu, C. C. Seaton and K. M. Ryan, *J. Am. Chem. Soc.*, 2014, **136**, 7954.
60 X. Y. Zhang, Y. Xu, J. J. Zhang, S. Dong, L. M. Shen, A. Gupta and N. Z. Bao, *Sci. Rep.*, 2018, **8**, 248.
61 Y. Liu, D. Q. Yin and M. T. Swihart, *Chem. Mater.*, 2018, **30**, 1399.
62 P. Vashishtha, G. V. Nutan, B. E. Griffith, Y. A. Fang, D. Giovanni, M. Jagadeeswararao, T. C. Sum, N. Mathews, S. G. Mhaisalkar, J. V. Hanna and T. White, *Chem. Mater.*, 2019, **31**, 9003.
63 M. G. Li, F. Y. Tian, T. S. Lin, L. Tao, X. Guo, Y. G. Chao, Z. Q. Guo, Q. H. Zhang, L. Gu, W. W. Yang, Y. S. Yu and S. J. Guo, *Small Methods*, 2021, **5**, 2100154.
64 Y. Hong, T. Kim, J. Jo, B. Kim, H. Jin, H. Baik and K. Lee, *ACS Nano*, 2020, **14**, 11205.
65 C. Yang, Z. J. Wang, Y. H. Lv, R. H. Yuan, Y. H. Wu and W. H. Zhang, *Chem. Eng. J.*, 2021, **406**, 126855.
66 S. W. Hsu, C. Ngo, W. Bryks and A. R. Tao, *Chem. Mater.*, 2015, **27**, 4957.
67 W. H. Li, R. Zamani, P. R. Gil, B. Pelaz, M. Ibanez, D. Cadavid, A. Shavel, R. A. Alvarez-Puebla, W. J. Parak, J. Arbiol and A. Cabot, *J. Am. Chem. Soc.*, 2013, **135**, 7098.
68 S. Deka, A. Genovese, Y. Zhang, K. Miszta, G. Bertoni, R. Krahne, C. Giannini and L. Manna, *J. Am. Chem. Soc.*, 2010, **132**, 8912.
69 A. E. Henkes and R. E. Schaak, *Chem. Mater.*, 2007, **19**, 4234.
70 B. Koo, R. N. Patel and B. A. Korgel, *Chem. Mater.*, 2009, **21**, 1962.
71 G. S. Shanker, A. Swarnkar, A. Chatterjee, S. Chakraborty, M. Phukan, N. Parveen, K. Biswas and A. Nag, *Nanoscale*, 2015, **7**, 9204.
72 Z. W. Wang, C. Schliehe, T. Wang, Y. Nagaoka, Y. C. Cao, W. A. Bassett, H. M. Wu, H. Y. Fan and H. Weller, *J. Am. Chem. Soc.*, 2011, **133**, 14484.
73 C. Schliehe, B. H. Juarez, M. Pelletier, S. Jander, D. Greshnykh, M. Nagel, A. Meyer, S. Foerster, A. Kornowski, C. Klinke and H. Weller, *Science*, 2010, **329**, 550.
74 Y. P. Du, Z. Y. Yin, J. X. Zhu, X. Huang, X. J. Wu, Z. Y. Zeng, Q. Y. Yan and H. Zhang, *Nat. Commun.*, 2012, **3**, 1177.
75 F. D. Wang, Y. Y. Wang, Y. H. Liu, P. J. Morrison, R. A. Loomis and W. E. Buhro, *Acc. Chem. Res.*, 2015, **48**, 13.
76 J. Lauth, F. E. S. Gorris, M. S. Khoshkhoo, T. Chasse, W. Friedrich, V. Lebedeya, A. Meyer, C. Klinke, A. Komowsld, M. Scheele and H. Weller, *Chem. Mater.*, 2016, **28**, 1728.
77 M. X. Liu, Y. Liu, B. B. Gu, X. B. Wei, G. X. Xu, X. M. Wang, M. T. Swihart and K. T. Yong, *Chem. Soc. Rev.*, 2019, **48**, 4950.
78 C. L. Johnson, E. Snoeck, M. Ezcurdia, B. Rodriguez-Gonzalez, I. Pastoriza-Santos, L. M. Liz-Marzan and M. J. Hytch, *Nat. Mater.*, 2008, **7**, 120.
79 Z. R. Guo, Y. Zhang, L. Huang, M. Wang, J. Wang, J. F. Sun, L. N. Xu and N. Gu, *J. Colloid Interface Sci.*, 2007, **309**, 518.
80 I. Pastoriza-Santos, R. A. Alvarez-Puebla and L. M. Liz-Marzan, *Eur. J. Inorg. Chem.*, 2010, 4288, DOI: 10.1002/ejic.201000575.
81 T. C. R. Rocha, H. Winnischofer, E. Westphal and D. Zanchet, *J. Phys. Chem. C*, 2007, **111**, 2885.
82 R. Tan, Y. C. Yuan, Y. Nagaoka, D. Eggert, X. D. Wang, S. Thota, P. Guo, H. R. Yang, J. Zhao and O. Chen, *Chem. Mater.*, 2017, **29**, 4097.

Open Access Article. Published on 27 January 2022. Downloaded on 11/30/2025 6:59:56 AM. This article is licensed under a Creative Commons Attribution 3.0 Unported Licence.

83 L. Manna, D. J. Milliron, A. Meisel, E. C. Scher and A. P. Alivisatos, *Nat. Mater.*, 2003, **2**, 382.
84 S. Ghosh, R. Gaspari, G. Bertoni, M. C. Spadaro, M. Prato, S. Turner, A. Cavalli, L. Manna and R. Brescia, *ACS Nano*, 2015, **9**, 8537.
85 N. L. Yang, Z. C. Zhang, B. Chen, Y. Huang, J. Z. Chen, Z. C. Lai, Y. Chen, M. Sindoro, A. L. Wang, H. F. Cheng, Z. X. Fan, X. Z. Liu, B. Li, Y. Zong, L. Gu and H. Zhang, *Adv. Mater.*, 2017, **29**, 1700769.
86 A. W. Tang, Z. L. Hu, Z. Yin, H. H. Ye, C. H. Yang and F. Teng, *Dalton Trans.*, 2015, **44**, 9251.
87 D. H. Li, J. Sun, X. Zhao and X. R. Yang, *Nanoscale*, 2015, **7**, 13191.
88 Z. Tang, H. Kwon, M. Y. Yi, K. Kim, J. W. Han, W. S. Kim and T. Yu, *ChemistrySelect*, 2017, **2**, 4655.
89 X. L. Wang, X. Liu, D. Q. Yin, Y. J. Ke and M. T. Swihart, *Chem. Mater.*, 2015, **27**, 3378.
90 Y. Zhai and M. Shim, *Chem. Mater.*, 2017, **29**, 2390.
91 W. van der Stam, Q. A. Akkerman, X. X. Ke, M. A. van Huis, S. Bals and C. D. Donega, *Chem. Mater.*, 2015, **27**, 283.
92 X. M. Li, H. B. Shen, J. Z. Niu, Y. G. Zhang, H. Z. Wang and L. S. Li, *J. Am. Chem. Soc.*, 2010, **132**, 12778.
93 L. X. Yi and M. Y. Gao, *Cryst. Growth Des.*, 2011, **11**, 1109.
94 W. Bryks, E. Lupi, C. Ngo and A. R. Tao, *J. Am. Chem. Soc.*, 2016, **138**, 13717.
95 W. Y. Wu, S. Chakrabortty, C. K. L. Chang, A. Guchhait, M. Lin and Y. Chan, *Chem. Mater.*, 2014, **26**, 6120.
96 V. Lesnyak, C. George, A. Genovese, M. Prato, A. Casu, S. Ayyappan, A. Scarpellini and L. Manna, *ACS Nano*, 2014, **8**, 8407.
97 Y. Liu, D. Q. Yin and M. T. Swihart, *Chem. Mater.*, 2018, **30**, 8089.
98 Z. Li, M. Saruyama, T. Asaka, Y. Tatetsu and T. Teranishi, *Science*, 2021, **373**, 332.
99 L. De Trizio and L. Manna, *Chem. Rev.*, 2016, **116**, 10852.
100 L. J. Mu, F. D. Wang and W. E. Buhro, *Chem. Mater.*, 2017, **29**, 3686.
101 P. Ramasamy, M. Kim, H. S. Ra, J. Kim and J. S. Lee, *Nanoscale*, 2016, **8**, 7906.
102 A. H. Khan, S. Pal, A. Dalui, B. Pradhan, D. D. Sarma and S. Acharya, *J. Mater. Chem. A*, 2019, **7**, 9782.
103 Y. Liu, C. K. Lim, Z. Fu, D. Q. Yin and M. T. Swihart, *Chem. Mater.*, 2019, **31**, 5706.
104 J. L. Fenton, B. C. Steimle and R. E. Schaak, *Inorg. Chem.*, 2019, **58**, 672.
105 A. E. Powell, J. M. Hodges and R. E. Schaak, *J. Am. Chem. Soc.*, 2016, **138**, 471.
106 A. Wolf, T. Kodanek and D. Dorfs, *Nanoscale*, 2015, **7**, 19519.
107 D. Yoon, S. Yoo, K. S. Nam, H. Baik, K. Lee and Q. H. Park, *Small*, 2016, **12**, 5728.
108 J. Park, J. Park, J. Lee, A. Oh, H. Baik and K. Lee, *ACS Nano*, 2018, **12**, 7996.
109 T. Kim, J. Park, Y. Hong, A. Oh, H. Baik and K. Lee, *ACS Nano*, 2019, **13**, 11834.
110 L. J. Mu, F. D. Wang, B. Sadtler, R. A. Loomis and W. E. Buhro, *ACS Nano*, 2015, **9**, 7419.
111 Y. D. Yin, R. M. Rioux, C. K. Erdonmez, S. Hughes, G. A. Somorjai and A. P. Alivisatos, *Science*, 2004, **304**, 711.
112 S. E. Moosavifard, S. Fani and M. Rahmanian, *Chem. Commun.*, 2016, **52**, 4517.
113 S. Koh, W. D. Kim, W. K. Bae, Y. K. Lee and D. C. Lee, *Chem. Mater.*, 2019, **31**, 1990.
114 C. W. Dong, D. Yao, J. Y. Feng, T. T. Huang, X. Y. Hu, Z. N. Wu, Y. Liu, B. Yang and H. Zhang, *Chem. Mater.*, 2016, **28**, 9139.
115 R. Lesyuk, E. Klein, I. Yaremchuk and C. Klinke, *Nanoscale*, 2018, **10**, 20640.
116 Y. Wang, Y. X. Hu, Q. Zhang, J. P. Ge, Z. D. Lu, Y. B. Hou and Y. D. Yin, *Inorg. Chem.*, 2010, **49**, 6601.
117 Y. Xie, L. Carbone, C. Nobile, V. Grillo, S. D'Agostino, F. Della Sala, C. Giannini, D. Altamura, C. Oelsner, C. Kryschi and P. D. Cozzoli, *ACS Nano*, 2013, **7**, 7352.
118 W. H. Li, A. Shavel, R. Guzman, J. Rubio-Garcia, C. Flox, J. D. Fan, D. Cadavid, M. Ibanez, J. Arbiol, J. R. Morante and A. Cabot, *Chem. Commun.*, 2011, **47**, 10332.
119 M. X. Liu, X. Z. Xue, C. Ghosh, X. Liu, Y. Liu, E. P. Furlani, M. T. Swihart and P. N. Prasad, *Chem. Mater.*, 2015, **27**, 2584.
120 X. L. Wang, Y. J. Ke, H. Y. Pan, K. Ma, Q. Q. Xiao, D. Q. Yin, G. Wu and M. T. Swihart, *ACS Catal.*, 2015, **5**, 2534.
121 Z. T. Deng, M. Mansuripur and A. J. Muscat, *J. Mater. Chem.*, 2009, **19**, 6201.
122 X. J. Wu, X. Huang, J. Q. Liu, H. Li, J. Yang, B. Li, W. Huang and H. Zhang, *Angew. Chem., Int. Ed.*, 2014, **53**, 5083.
123 R. W. Lord, J. Fanghanel, C. F. Holder, I. Dabo and R. E. Schaak, *Chem. Mater.*, 2020, **32**, 10227.
124 C. M. Hessel, V. P. Pattani, M. Rasch, M. G. Panthani, B. Koo, J. W. Tunnell and B. A. Korgel, *Nano Lett.*, 2011, **11**, 2560.
125 J. Choi, N. Kang, H. Y. Yang, H. J. Kim and S. U. Son, *Chem. Mater.*, 2010, **22**, 3586.
126 H. B. Li, R. Brescia, M. Povia, M. Prato, G. Bertoni, L. Manna and I. Moreels, *J. Am. Chem. Soc.*, 2013, **135**, 12270.
127 E. H. Robinson, K. M. Dwyer, A. C. Koziel, A. Y. Nuriye and J. E. Macdonald, *Nanoscale*, 2020, **12**, 23036.
128 D. X. Zhu, A. W. Tang, Q. H. Kong, B. Zeng, C. H. Yang and F. Teng, *J. Phys. Chem. C*, 2017, **121**, 15922.
129 J. Xu, X. Yang, Q. D. Yang, W. J. Zhang and C. S. Lee, *ACS Appl. Mater. Interfaces*, 2014, **6**, 16352.
130 D. Y. Xu, S. L. Shen, Y. J. Zhang, H. W. Gu and Q. B. Wang, *Inorg. Chem.*, 2013, **52**, 12958.
131 G. Gabka, P. Bujak, A. Ostrowski, W. Tomaszewski, W. Lisowski, J. W. Sobczak and A. Pron, *Inorg. Chem.*, 2016, **55**, 6660.
132 X. T. Lu, Z. B. Zhuang, Q. Peng and Y. D. Li, *Chem. Commun.*, 2011, **47**, 3141.

 This journal is © The Royal Society of Chemistry 2022

Open Access Article. Published on 27 January 2022. Downloaded on 11/30/2025 6:59:56 AM.
This article is licensed under a Creative Commons Attribution 3.0 Unported Licence.

133 H. Ren, Z. Li, Y. W. Sun, P. Gao, C. McCarthy, N. Liu, H. X. Xu and K. M. Ryan, *Chem. Mater.*, 2020, **32**, 7254.
134 G. Manna, R. Bose and N. Pradhan, *Angew. Chem., Int. Ed.*, 2013, **52**, 6762.
135 J. F. Liu, M. Meyns, T. Zhang, J. Arbiol, A. Cabot and A. Shavel, *Chem. Mater.*, 2018, **30**, 1799.
136 A. G. Rachkov and A. M. Schimpf, *Chem. Mater.*, 2021, **33**, 1394.
137 T.-H. Le, S. Lee, H. Jo, M. Kim, J. Lee, M. Chang and H. Yoon, *ACS Appl. Nano Mater.*, 2021, **4**, 7621.
138 J. Wang, X. C. Guo, Y. He, M. J. Jiang and R. Sun, *RSC Adv.*, 2017, **7**, 40249.
139 W. Luc, X. B. Fu, J. J. Shi, J. J. Lv, M. Jouny, B. H. Ko, Y. B. Xu, Q. Tu, X. B. Hu, J. S. Wu, Q. Yue, Y. Y. Liu, F. Jiao and Y. J. Kang, *Nat. Catal.*, 2019, **2**, 423.
140 I. Pastoriza-Santos, A. Sanchez-Iglesias, B. Rodriguez-Gonzalez and L. M. Liz-Marzan, *Small*, 2009, **5**, 440.
141 T. Balkan, H. Kucukkececi, H. Zarenezhad, S. Kaya and O. Metin, *J. Alloys Compd.*, 2020, **831**, 154787.
142 S. Singh, P. Liu, A. Singh, C. Coughlan, J. J. Wang, M. Lusi and K. M. Ryan, *Chem. Mater.*, 2015, **27**, 4742.
143 B. A. Tappan and R. L. Brutchey, *ChemNanoMat*, 2020, **6**, 1567.
144 D. J. Chakrabarti and D. E. Laughlin, *Bull. Alloy Phase Diagrams*, 1983, **4**, 254.
145 Y. He, T. S. Zhang, X. Shi, S. H. Wei and L. D. Chen, *NPG Asia Mater.*, 2015, **7**, 210.
146 C. Nethravathi, C. R. Rajamathi, M. Rajamathi, R. Maki, T. Mori, D. Golberg and Y. Bando, *J. Mater. Chem. A*, 2014, **2**, 985.
147 J. Xu, X. Yang, Q. D. Yang, X. Huang, Y. B. Tang, W. J. Zhang and C. S. Lee, *Chem. – Asian J.*, 2015, **10**, 1490.
148 K. M. Koskela, M. J. Strumolo and R. L. Brutchey, *Trends Chem.*, 2021, **3**, 1061.
149 J. C. Sarker and G. Hogarth, *Chem. Rev.*, 2021, **121**, 6057.
150 A. F. Harper, M. L. Evans and A. J. Morris, *Chem. Mater.*, 2020, **32**, 6629.
151 Z. H. Guo, J. Z. Li, R. K. Pan, J. J. Cheng, R. Chen and T. C. He, *Nanoscale*, 2020, **12**, 15560.
152 Y. Dai, S. J. Liu and N. F. Zheng, *J. Am. Chem. Soc.*, 2014, **136**, 5583.
153 K. Tanabe, *Mater. Lett.*, 2007, **61**, 4573.
154 Y. N. Wijaya, J. Kim, W. M. Choi, S. H. Park and M. H. Kim, *Nanoscale*, 2017, **9**, 11705.
155 Z. Q. Shi, J. T. Tang, L. Chen, C. R. Yan, S. Tanvir, W. A. Anderson, R. M. Berry and K. C. Tam, *J. Mater. Chem. B*, 2015, **3**, 603.
156 H. Y. Zhu, S. Zhang, S. J. Guo, D. Su and S. H. Sun, *J. Am. Chem. Soc.*, 2013, **135**, 7130.
157 S. Thota, Y. C. Wang and J. Zhao, *Mater. Chem. Front.*, 2018, **2**, 1074.
158 J. Monzo, Y. Malewski, R. Kortlever, F. J. Vidal-Iglesias, J. Solla-Gullon, M. T. M. Koper and P. Rodriguez, *J. Mater. Chem. A*, 2015, **3**, 23690.
159 J. Jiang, S. Yoon and L. Piao, *CrystEngComm*, 2020, **22**, 4386.
160 X. Q. Huang, S. H. Tang, X. L. Mu, Y. Dai, G. X. Chen, Z. Y. Zhou, F. X. Ruan, Z. L. Yang and N. F. Zheng, *Nat. Nanotechnol.*, 2011, **6**, 28.
161 K. W. Zhang, T. X. Song, C. Wang, H. M. You, B. Zou, S. Y. Guo, Y. K. Du and S. J. Li, *Inorg. Chem.*, 2021, **60**, 7527.
162 H. Y. Jin, C. X. Guo, X. Liu, J. L. Liu, A. Vasileff, Y. Jiao, Y. Zheng and S. Z. Qiao, *Chem. Rev.*, 2018, **118**, 6337.
163 Y. Zhang, C. C. Xing, Y. Liu, M. C. Spadaro, X. Wang, M. Y. Li, K. Xiao, T. Zhang, P. Guardia, K. H. Lim, A. O. Moghaddam, J. Llorca, J. Arbiol, M. Ibanez and A. Cabot, *Nano Energy*, 2021, **85**, 105991.
164 Y. Liu, X. K. Zeng, X. Y. Hu, J. Hu and X. W. Zhang, *J. Chem. Technol. Biotechnol.*, 2019, **94**, 22.
165 D. H. Deng, K. S. Novoselov, Q. Fu, N. F. Zheng, Z. Q. Tian and X. H. Bao, *Nat. Nanotechnol.*, 2016, **11**, 218.
166 Z. X. Zhang, K. P. Zhao, T. R. Wei, P. F. Qiu, L. D. Chen and X. Shi, *Energy Environ. Sci.*, 2020, **13**, 3307.
167 P. F. Qiu, X. Shi and L. D. Chen, *Energy Storage Mater.*, 2016, **3**, 85.
168 J. Wu, Y. B. Chen, J. Q. Wu and K. Hippalgaonkar, *Adv. Electron. Mater.*, 2018, **4**, 1800248.
169 Q. Wang, J. H. Li and J. J. Li, *Phys. Chem. Chem. Phys.*, 2018, **20**, 1460.
170 B. Peng, H. Zhang, H. Z. Shao, K. Xu, G. Ni, J. Li, H. Y. Zhu and C. M. Soukoulis, *J. Mater. Chem. A*, 2018, **6**, 2018.
171 M. Q. Sun, N. Kreis, K. X. Chen, X. Q. Fu, S. Guo and H. Wang, *Chem. Mater.*, 2021, **33**, 8546.
172 R. M. Cordova-Castro, M. Casavola, M. van Schilfgaarde, A. V. Krasavin, M. A. Green, D. Richards and A. V. Zayats, *ACS Nano*, 2019, **13**, 6550.
173 T. X. Wei, Y. F. Liu, W. J. Dong, Y. Zhang, C. Y. Huang, Y. Sun, X. Chen and N. Dai, *ACS Appl. Mater. Interfaces*, 2013, **5**, 10473.
174 G. N. Liu, S. P. Qi, J. X. Chen, Y. B. Lou, Y. X. Zhao and C. Burda, *Nano Lett.*, 2021, **21**, 2610.
175 X. Liu and M. T. Swihart, *Chem. Soc. Rev.*, 2014, **43**, 3908.
176 A. Comin and L. Manna, *Chem. Soc. Rev.*, 2014, **43**, 3957.
177 J. A. Faucheaux, A. L. D. Stanton and P. K. Jain, *J. Phys. Chem. Lett.*, 2014, **5**, 976.
178 T. Sun, Y. J. Wang, W. Z. Yu, Y. S. Wang, Z. G. Dai, Z. K. Liu, B. N. Shivananju, Y. P. Zhang, K. Fu, B. Shabbir, W. L. Ma, S. J. Li and Q. L. Bao, *Small*, 2017, **13**, 1701881.
179 S. W. Hsu, K. On and A. R. Tao, *J. Am. Chem. Soc.*, 2011, **133**, 19072.
180 L. H. Chen, H. F. Hu, Y. Z. Chen, J. Gao and G. H. Li, *Mater. Adv.*, 2021, **2**, 907.
181 Y. Liu, M. Liu and M. T. Swihart, *J. Phys. Chem. C*, 2017, **121**, 13435.
182 C. Hu, W. H. Chen, Y. Xie, S. K. Verma, P. Destro, G. Zhan, X. Z. Chen, X. J. Zhao, P. J. Schuck, I. Kriegel and L. Manna, *Nanoscale*, 2018, **10**, 2781.
183 Y. Yao, A. Bhargava and R. D. Robinson, *Chem. Mater.*, 2021, **33**, 608.

Open Access Article. Published on 27 January 2022. Downloaded on 11/30/2025 6:59:56 AM.
This article is licensed under a Creative Commons Attribution 3.0 Unported Licence.

184 W. D. Liu, L. Yang and Z. G. Chen, *Nano Today*, 2020, **35**, 100938.
185 B. Gahtori, S. Bathula, K. Tyagi, M. Jayasimhadri, A. K. Srivastava, S. Singh, R. C. Budhani and A. Dhar, *Nano Energy*, 2015, **13**, 36.
186 Y. Liu, Y. Zhang, S. Ortega, M. Ibanez, K. H. Lim, A. Grau-Carbonell, S. Marti-Sanchez, K. M. Ng, J. Arbiol, M. V. Kovalenko, D. Cadavid and A. Cabot, *Nano Lett.*, 2018, **18**, 2557.
187 S. Ortega, M. Ibanez, Y. Liu, Y. Zhang, M. V. Kovalenko, D. Cadavid and A. Cabot, *Chem. Soc. Rev.*, 2017, **46**, 3510.
188 R. Freer and A. V. Powell, *J. Mater. Chem. C*, 2020, **8**, 441.
189 K. P. Zhao, P. F. Qiu, Q. F. Song, A. B. Blichfeld, E. Eikeland, D. D. Ren, B. H. Ge, B. B. Iversen, X. Shi and L. D. Chen, *Mater. Today Phys.*, 2017, **1**, 14.
190 L. Yang, Z. G. Chen, G. Han, M. Hong, Y. C. Zou and J. Zou, *Nano Energy*, 2015, **16**, 367.
191 W. W. Liao, L. Yang, J. Chen, D. L. Zhou, X. L. Qu, K. Zheng, G. Han, J. B. Zhou, M. Hong and Z. G. Chen, *Chem. Eng. J.*, 2019, **371**, 593.
192 Y. He, T. Day, T. S. Zhang, H. L. Liu, X. Shi, L. D. Chen and G. J. Snyder, *Adv. Mater.*, 2014, **26**, 3974.
193 J. B. Yu, T. W. Li, G. Nie, B. P. Zhang and Q. Sun, *Nanoscale*, 2019, **11**, 10306.
194 T. Mao, P. F. Qiu, P. Hu, X. L. Du, K. P. Zhao, T. R. Wei, J. Xiao, X. Shi and L. D. Chen, *Adv. Sci.*, 2020, **7**, 1901598.
195 M. Y. Li, Y. Liu, Y. Zhang, X. Han, T. Zhang, Y. Zuo, C. Y. Xie, K. Xiao, J. Arbiol, J. Llorca, M. Ibanez, J. F. Liu and A. Cabot, *ACS Nano*, 2021, **15**, 4967.
196 X. L. Yu, D. Wang, J. L. Liu, Z. S. Luo, R. F. Du, L. M. Liu, G. J. Zhang, Y. H. Zhang and A. Cabot, *J. Phys. Chem. C*, 2016, **120**, 24265.
197 Y. Liu, H. G. Zhang, P. K. Behara, X. Y. Wang, D. W. Zhu, S. Ding, S. P. Ganesh, M. Dupuis, G. Wu and M. T. Swihart, *ACS Appl. Mater. Interfaces*, 2018, **10**, 42417.
198 X. Shao, T. Y. Zhang, B. Li, Y. Wu, X. Y. Ma, J. C. Wang and S. Jiang, *CrystEngComm*, 2020, **22**, 678.
199 H. Y. Zou, M. X. Gao, T. Yang, Q. L. Zeng, X. X. Yang, F. Liu, M. T. Swihart, N. Li and C. Z. Huang, *Phys. Chem. Chem. Phys.*, 2017, **19**, 6964.
200 A. Dutta, S. K. Dutta, S. K. Mehetor, I. Mondal, U. Pal and N. Pradhan, *Chem. Mater.*, 2016, **28**, 1872.
201 S. L. Zhao, Y. Wang, Q. H. Zhang, Y. F. Li, L. Gu, Z. H. Dai, S. L. Liu, Y. Q. Lan, M. Han and J. C. Bao, *Inorg. Chem. Front.*, 2016, **3**, 1501.
202 Q. Li, X. F. Wang, K. Tang, M. F. Wang, C. Wang and C. L. Yan, *ACS Nano*, 2017, **11**, 12230.
203 Y. Liu, J. D. Wu, Y. H. Jin, W. Y. Zhen, Y. H. Wang, J. H. Liu, L. H. Jin, S. T. Zhang, Y. Zhao, S. Y. Song, Y. Yang and H. J. Zhang, *Adv. Funct. Mater.*, 2019, **29**, 1904678.
204 S. Vikulov, F. Di Stasio, L. Ceseracciu, P. L. Saldanha, A. Scarpellini, Z. Y. Dang, R. Krahne, L. Manna and V. Lesnyak, *Adv. Funct. Mater.*, 2016, **26**, 3670.
205 D. Yoon, H. Jin, S. Ryu, S. Park, H. Baik, S. J. Oh, S. Haam, C. Joo and K. Lee, *CrystEngComm*, 2015, **17**, 4627.
206 J. He, L. S. Ai, X. Liu, H. Huang, Y. B. Li, M. G. Zhang, Q. R. Zhao, X. G. Wang, W. Chen and H. S. Gu, *J. Mater. Chem. B*, 2018, **6**, 1035.
207 J. Just, C. Coughlan, S. Singh, H. Ren, O. Muller, P. Becker, T. Unold and K. M. Ryan, *ACS Nano*, 2021, **15**, 6439.
208 V. K. Ravi, S. Saikia, S. Yadav, V. V. Nawale and A. Nag, *ACS Energy Lett.*, 2020, **5**, 1794.


This journal is © The Royal Society of Chemistry 2022